Monthly Notices of the ROYAL ASTRONOMICAL SOCIETY

MNRAS **525,** 5575–5596 (2023) https://doi.org/10.1093/mnras/stad2603
Advance Access publication 2023 September 13

A striking relationship between dust extinction and radio detection in DESI QSOs: evidence for a dusty blow-out phase in red QSOs

V. A. Fawcett [1,2★] D. M. Alexander [2] A. Brodzeller [3] A. C. Edge,[2] D. J. Rosario,[1,2] A. D. Myers,[4] J. Aguilar,[5] S. Ahlen,[6] R. Alfarsy,[7] D. Brooks,[8] R. Canning,[7] C. Circosta,[8] K. Dawson,[3] A. de la Macorra,[9] P. Doel,[8] K. Fanning,[10] A. Font-Ribera,[11] J. E. Forero-Romero,[12] S. Gontcho A Gontcho,[5] J. Guy,[5] C. M. Harrison,[1] K. Honscheid,[10,13,14] S. Juneau,[15] R. Kehoe,[16] T. Kisner,[5] A. Kremin,[5] M. Landriau,[5] M. Manera,[11] A. M. Meisner,[15] R. Miquel,[11,17] J. Moustakas,[18] J. Nie,[19] W. J. Percival,[20,21,22] C. Poppett,[5,23,24] R. Pucha,[25] G. Rossi,[26] D. Schlegel,[5] M. Siudek,[11,27] G. Tarlé,[28] B. A. Weaver,[15] Z. Zhou[19] and H. Zou[19]

Affiliations are listed at the end of the paper

Accepted 2023 August 24. Received 2023 August 21; in original form 2023 May 15

ABSTRACT

We present the first eight months of data from our secondary target programme within the ongoing Dark Energy Spectroscopic Instrument (DESI) survey. Our programme uses a mid-infrared and optical colour selection to preferentially target dust-reddened quasi-stellar objects (QSOs) that would have otherwise been missed by the nominal DESI QSO selection. So far, we have obtained optical spectra for 3038 candidates, of which ∼70 per cent of the high-quality objects (those with robust redshifts) are visually confirmed to be Type 1 QSOs, consistent with the expected fraction from the main DESI QSO survey. By fitting a dust-reddened blue QSO composite to the QSO spectra, we find they are well-fitted by a normal QSO with up to $A_V \sim 4$ mag of line-of-sight dust extinction. Utilizing radio data from the LOFAR Two-metre Sky Survey (LoTSS) DR2, we identify a striking positive relationship between the amount of line-of-sight dust extinction towards a QSO and the radio detection fraction, that is not driven by radio-loud systems, redshift and/or luminosity effects. This demonstrates an intrinsic connection between dust reddening and the production of radio emission in QSOs, whereby the radio emission is most likely due to low-powered jets or winds/outflows causing shocks in a dusty environment. On the basis of this evidence, we suggest that red QSOs may represent a transitional 'blow-out' phase in the evolution of QSOs, where winds and outflows evacuate the dust and gas to reveal an unobscured blue QSO.

Key words: galaxies: active – galaxies: evolution – quasars: general – quasars: supermassive black holes – radio continuum: galaxies.

1 INTRODUCTION

Quasi-stellar objects (QSOs), also known as quasars, are the most powerful class of active galactic nuclei (AGN), with extremely high bolometric luminosities (10^{45}–10^{48} erg s^{-1}). These high luminosities are now known to be due to mass accretion onto a supermassive black-hole (SMBH; masses of 10^7–10^9 M$_\odot$). The observed correlation between the masses of SMBHs at the centres of spheroidal galaxies and the bulge mass of the hosting galaxy suggests an intrinsic link between the growth of the SMBH and the surrounding host galaxy (Kormendy & Ho 2013).

A canonical model for this growth phase invokes gas-rich major mergers (Sanders et al. 1988; Hopkins et al. 2008; Alexander & Hickox 2012) in which rapid gas inflow to the nucleus fuels a powerful QSO, obscured in its early stages by a high column of gas and dust. Through powerful winds and/or outflows, an unobscured 'typical' blue QSO is eventually revealed. However, it is still unclear what type of object represents the transitional 'blow-out' stage between the obscured and unobscured QSO phase. Potential candidates include (1) the well-studied dust obscured 'red QSOs' (e.g. White et al. 2003; Glikman et al. 2004, 2007; Maddox et al. 2008; Klindt et al. 2019), selected as broad line QSOs with red optical or near-infrared (NIR) colours (2) 'broad absorption line quasars' (BALQSOs; e.g. Weymann et al. 1991; Morabito et al. 2019; Petley et al. 2022), which display broad absorption typically blueward of the C IV emission line and (3) the rarer 'extremely red quasars' (ERQs; e.g. Ross et al. 2015; Hamann et al. 2017), selected to have red optical–mid-infrared (MIR) colours. All of these objects are thought to play an important role in the regulation of star formation in the host galaxy (otherwise known as 'AGN feedback'; see reviews by Heckman & Best 2014 and Harrison et al. 2018).

Over recent years, a number of groups have explored whether red QSOs represent a transitional blow-out phase, determining their

★ E-mail: vicky.fawcett@newcastle.ac.uk

properties and how they relate to typical blue QSOs (Richards et al. 2003; Glikman et al. 2004, 2007, 2012, 2022; Georgakakis et al. 2009; Urrutia et al. 2009; Banerji et al. 2012, 2015; Kim & Im 2018; Klindt et al. 2019; Fawcett et al. 2020, 2021, 2022; Rosario et al. 2020, 2021; Calistro Rivera et al. 2021; Petter et al. 2022; Stacey et al. 2022). In our recent work, we have shown that the majority of red QSOs from the Sloan Digital Sky Survey (SDSS; York et al. 2000), selected based on their optical g–i colour, are red due to line-of-sight dust extinction (Calistro Rivera et al. 2021; Fawcett et al. 2022). Somewhat surprisingly, we found that red QSOs exhibited enhanced radio emission, compared to blue QSOs, which is typically compact (<2 kpc; Klindt et al. 2019; Fawcett et al. 2020; Rosario et al. 2020, 2021) and peaks around the radio-quiet/radio-loud threshold (Fawcett et al. 2020; Rosario et al. 2020). The observed differences in the radio properties of red and blue QSOs do not appear to be associated with any differences in the star formation (Fawcett et al. 2020; Calistro Rivera et al. 2021; Andonie et al. 2022), accretion (Klindt et al. 2019; Fawcett et al. 2022), or large scale structure (Petter et al. 2022) properties between the two populations. On the basis of these results, a potential self-consistent scenario that links the enhanced radio emission to the dust in red QSOs is that the radio emission is due to shocks produced by either an outflow or a jet interacting with a higher opacity interstellar medium (ISM)/circumnuclear environment. These outflows/jets could also potentially drive out the surrounding gas and dust (i.e. AGN feedback), eventually revealing a typical blue QSO therefore red QSOs are prime candidates for an intermediate stage in the evolution of QSOs.

It is worth noting that the measured dust extinctions towards optically selected SDSS red QSOs are modest ($A_V < 0.7$ mag; Calistro Rivera et al. 2021; Fawcett et al. 2022) and they likely represent the tip of the iceberg of a larger, more heavily reddened QSO population. Indeed, other studies have utilized NIR photometry in order to select more heavily reddened red QSO samples (e.g. Glikman et al. 2004, 2007; Banerji et al. 2015; Glikman et al. 2022), with measured dust extinctions up to $A_V \sim 5$ mag. For example, Glikman et al. (2022) used a *WISE*–2MASS colour selection to define a sample of red QSOs with dust extinctions $E(B-V) > 0.25$ mag ($A_V \gtrsim 0.8$ mag).[1] Utilizing radio data from both the Faint Images of the Radio Sky at Twenty-centimeters (FIRST; Becker, White & Helfand 1995) and the Very Large Array Sky Survey (VLASS; Gordon et al. 2020), they found a higher radio detection fraction for their red QSOs compared to a blue QSO sample [$E(B-V) < 0.25$ mag], in addition to a higher fraction of compact radio morphologies for the red QSOs in both radio data sets. These results are remarkably similar to our less reddened optically selected red QSOs (Klindt et al. 2019; Fawcett et al. 2020; Rosario et al. 2020).

A limitation of our previous red QSO studies is the shallow magnitude limit of SDSS which restricts us to the most luminous and optically brightest objects, with only modest amounts of extinction. We therefore require larger, fainter, and redder samples of QSOs to robustly test whether red QSOs represent a transitional phase in the evolution of QSOs: the Dark Energy Spectroscopic Instrument (DESI; DESI Collaboration et al. 2016a, b) has the capability to do just this. DESI has completed the first year of a five-year survey which aims to obtain optical spectra for ∼3 million QSOs down to $r \sim 23.2$ mag (DESI Collaboration et al. 2022; Silber et al. 2023; Miller et al. in preparation). These data will be revolutionary in QSO science, pushing 1–2 mag fainter than SDSS and, consequently, identifying both more obscured and more typical systems (see section 5 of Alexander et al. 2023 for diversity in the QSO spectra).

The DESI QSO target selection consists of both an optical colour selection and a Random Forest selection (Yèche et al. 2020; Chaussidon et al. 2023).[2] Like any standard optical QSO selection, both the Random Forest and colour selection are biased towards optically blue QSOs since the majority of QSOs, and therefore the Random Forest training sets, are blue. This bias will inevitably select against the more 'exotic' and dust reddened QSO population. In 2020 October, a call for DESI proposals for 'secondary target' programmes was announced, with the aim of utilizing spare DESI fibres and expanding the DESI science beyond the key cosmological aims of the survey. Our group successfully proposed a programme (PI: V. Fawcett) which targets dust-reddened QSOs that have been missed by the nominal DESI QSO selections, with aims to (1) push to higher levels of dust extinction than can be identified by either the SDSS or the nominal DESI QSO selection, (2) determine whether the enhanced radio emission found in SDSS red QSOs extends to more heavily reddened systems, (3) explore the origin of the enhanced radio emission found in red QSOs, and (4) explore exotic sub-populations of QSOs within DESI.

In this first paper, we introduce and present the first eight months of data from our DESI secondary target programme and explore the connection between dust extinction and radio emission in DESI QSOs, using data from the LOFAR Two-metre Sky Survey (LoTSS) Data Release 2 (Shimwell et al. 2022). In Section 2, we describe our secondary target programme and in Section 3, we describe how our secondary target programme extends the nominal DESI QSO selection, the methods used in this paper, and the construction of our combined QSO sample which is used for the scientific analyses in this paper. In Section 4, we present our results and in Section 5, we discuss how our sample extends previous red QSO work and explore the origin of the radio emission. Unless specified otherwise, in this paper, we use AB magnitudes. Throughout our work, we adopt a flat λ-cosmology with $H_0 = 70\,\mathrm{km\,s^{-1}Mpc^{-1}}$, $\Omega_\mathrm{M} = 0.3$ and $\Omega_\lambda = 0.7$. The data underlying the figures in this paper are available online: https://doi.org/10.5281/zenodo.8147342.

2 SECONDARY TARGET PROGRAMME

In this section, we describe our secondary target selection and the DESI data (Section 2.1) and spectral classification method (Section 2.2).

2.1 Defining our secondary target programme selection

Our secondary target programme aims to expand the DESI QSO colour space, utilizing MIR data from the *Wide-field Infrared Survey Explorer* (*WISE*; Wright et al. 2010). The main goal of this programme is to build up a statistically significant sample of dust-reddened QSOs that may have otherwise been missed by the nominal DESI QSO selections. However, due to our optical colour selection (which we describe in more detail below), our programme will also select extremely blue QSOs. Therefore, it should be noted

[1] $A_V = R_V \times E(B-V)$; where R_V is the total-to-selective extinction, which determines the shape of the extinction curve (Cardelli, Clayton & Mathis 1989). For example, the Milky Way dust extinction curve has an $R_V = 3.1$ (Fitzpatrick 1999).

[2] The code for the various Survey Validation selections are publicly available on GitHub: https://github.com/desihub/desitarget/blob/0.51.0/py/desitarget/sv1/sv1_cuts.py

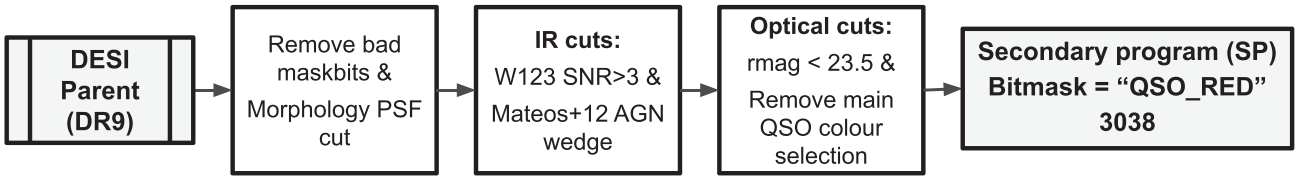

Figure 1. Flow chart illustrating the selection process for our DESI secondary programme (SP) sample. The DESI SP sample consists of objects that were specifically targeted by our secondary target programme; these must satisfy a morphology, magnitude, and *WISE* *W*123 signal-to-noise cut, have MIR colours consistent with the *WISE* Mateos et al. (2012) AGN wedge, and pass an optical colour–colour cut (see Fig. 2), resulting in 3038 objects that were observed. Each step is described in more detail in Section 2.1. An electronic table containing the DESI TARGETID for the full SP sample, and additionally the RA, Dec., redshift, spectype, and $L_{6\,\mu m}$ for the SP sample included in the DESI Early Data Release (DESI Collaboration et al. 2023), is available online. For the analyses in this paper, we further restrict the sample to visually confirm QSOs and combine with typical DESI QSOs, as is illustrated in Fig. 4.

that, although the BITMASK[3] assigned to the objects observed by our programme is QSO_RED, the sample will include a small fraction of optically blue QSOs, in addition to dust-reddened QSOs. For the analyses in this paper, our secondary target programme is solely used to boost the source statistics of the rarer dust-reddened QSOs and in combination with a larger nominal sample of DESI QSOs, the majority of which will be typical blue QSOs by selection.

Our current sample [which we refer to as the 'DESI secondary programme (SP) sample'] is taken from the first ∼8 months of observations, including all of the DESI Survey Validation (SV; DESI Collaboration et al. 2023) data (2020 December–2021 June) and part of the 'Main' survey data (2021 May–2021 July).[4] The DESI SV observations are split into three different targeting campaigns: 'SV1', 'SV2', and 'SV3'; our DESI SP sample only utilizes SV1 and SV3 observations since no secondary targets were assigned during SV2 (DESI Collaboration et al. 2023; Myers et al. 2023). During the SV3 phase, primary targets were prioritized for multiple observations before secondary targets were scheduled in order to obtain highly complete samples of DESI primary targets. Thus, a portion of our SP sample is biased towards the colours of primary DESI classes, particularly Luminous Red Galaxies (LRGs; Zhou et al. 2023; $z < 21.7$ limit in SV3) and QSOs (Chaussidon et al. 2023; $r < 23$ limit in SV3). This bias will gradually diminish over the course of the DESI Main survey, for which, our SP targets are assigned an observational priority at least as high as any other primary target (see section 5 of Schlafly et al. 2023). The flowchart in Fig. 1 displays our secondary target selection process, which we describe below.

A key distinguishing component of our SP compared to the DESI QSO sample is the MIR *WISE* selection. We first started with the DESI DR9 legacy photometric catalogues (Dey et al. 2019)[5], which contain optical photometry in the *g* (4730 Å), *r* (6420 Å), and *z* bands (9260 Å), as well as four MIR bands (at 3.4, 4.6, 12, and 22 μm) from stacks of *WISE/NEOWISE* data (Wright et al. 2010; Mainzer et al. 2011, 2014), referred to as unWISE coadds (Lang 2014; for more details see section 6 of Dey et al. 2019). We first used the MASKBIT column in order to remove objects with flagged photometric errors. In our selection, we remove objects with a MASKBIT corresponding to either BRIGHT (object touches the pixel of a bright star), ALLMASK_G, ALLMASK_R, ALLMASK_Z (object touches a bad pixel in either the *g*-, *r*-, or *z*-band images), BAILOUT (object touches a pixel in a region where source fitting failed), GALAXY (object touches a pixel in a large galaxy), or CLUSTER (object touches a pixel in a globular cluster).[6] These were chosen to be consistent with the nominal DESI QSO SV target selection (Chaussidon et al. 2023). We then applied a morphology cut, requiring either point sources ('PSF' morphology) or a small relative χ^2 difference between the PSF and more extended morphological models (defined in Chaussidon et al. 2023) from the DR9 legacy imaging (Dey et al. 2019; Schlegel et al. in preparation).

To ensure we minimize non-QSO contaminants in our sample, we required a signal-to-noise ratio (SNR) cut of >3 in the *WISE* *W*1, *W*2, and *W*3 bands and applied the Mateos et al. (2012) 'AGN wedge' (a *W*1–*W*2 and *W*2–*W*3 colour–colour selection). We chose to use the Mateos et al. (2012) wedge rather than more simple, liberal MIR cuts (e.g. Stern et al. 2012; $W1–W2 \geq 0.8$, Vega) in order to optimize the number of reliable QSOs observed by our SP, in addition to obtaining accurate *W*3 fluxes used to calculate the 6 μm luminosity (see Section 3.4). However, this may result in fewer sources observed which have MIR colours that lie outside of the AGN wedge (in particular, exotic QSOs with more extreme MIR colours or higher redshift QSOs for which the AGN wedge is known to be less reliable). After applying the MIR cuts, we then imposed an *r*-band magnitude cut of $r < 23.5$ mag (matching the more liberal cut used for the SV QSO selection). We further removed any object that falls within the region of *g*–*r* versus *r*–*z* colour–colour space that is the predominant colour selection for nominal DESI QSOs ($g–r < 1.3$ & $r–z > −0.4$ & $r–z < 1.1$; see Fig. 2), in order to expand the DESI QSO colour space. This resulted in predominantly red objects, although, as noted earlier, the selection also includes extremely blue objects (e.g. ∼12.3 per cent of our secondary programme QSOs have an $r–z < −0.4$; see Fig. 2). The nominal QSO selection includes a Random Forest selection that will also target QSOs outside this colour region, although these objects will be rare; see Fig. 5 and Yèche et al. 2020. The number of objects that both satisfy these criteria, and were specifically targeted by our programme, is 3038.[7] It is worth noting that if this programme continues for the full five years of the DESI

[3]Different types of targets are assigned different bits, which can then be accessed via the targeting bitmasks (e.g. DESI_TARGET). For example, in DESI, the QSO targets are assigned a desi_mask bit 2 and our secondary QSO_RED targets are assigned a scnd_mask bit 5. Therefore, the targets that are solely targeted by our programme would be selected by SCND_TARGET = 32 (≡ 2^5). For more information, see Myers et al. (2023).
[4]The DESI Early Data Release (EDR; DESI Collaboration et al. 2023) will only include observations from the SV period.
[5]https://www.legacysurvey.org/

[6]See https://www.legacysurvey.org/dr9/bitmasks/ for a detailed description of each maskbit.
[7]Note: an additional 25 objects were targeted by our programme but no longer meet our photometric selection criteria due to updated photometry. We do not include these 25 in the final DESI SP sample.

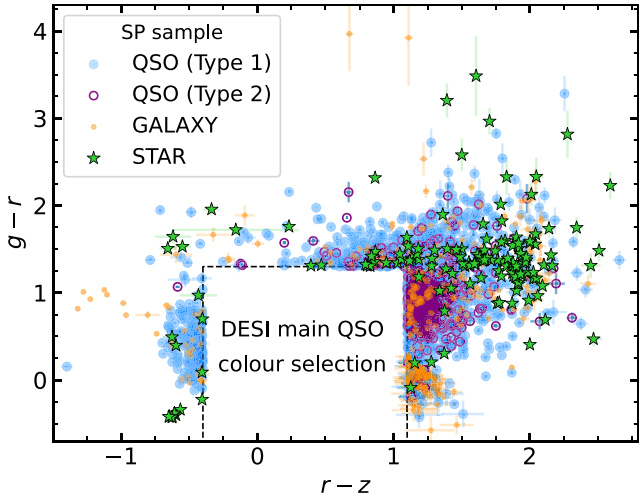

Figure 2. g–r versus r–z colour–colour distribution for our high-quality (VI_quality ≥ 2.5) SP sample split by spectral type determined from VI; QSOs (Type 1: blue dots; Type 2: purple circles), galaxies (orange dots), and stars (green stars). The region of colour space that is predominantly occupied by the nominally selected DESI QSOs is highlighted; we do not target any object in this region but instead combine our sample with the nominal DESI QSOs for some of the analyses in this paper (see Section 3.1). It is worth noting that the nominal DESI QSO selection also utilizes a Random Forest selection that will target QSOs outside of this main colour region (see Fig. 5).

survey, we expect over ∼8 times this number of SP targets to be observed.

2.2 Spectral classification

The DESI spectrograph covers an observed wavelength range of ∼3600–9800 Å, with a spectral resolution of ∼2000–5000 (blue to red). In order to measure the redshift and determine the spectral type (hereafter 'spectype') of each spectrum, DESI makes use of three tools. `redrock`[8] (Bailey et al. in preparation) is the standard DESI spectral template-fitting code that uses a set of templates to classify objects into one of three broad categories: QSO, GALAXY, and STAR. `redrock` uses a Bayesian approach and selects the best-fitting solutions based on the lowest reduced χ^2 values. In addition to `redrock`, DESI also utilizes two 'afterburner' codes that are applied after `redrock` is run: `QuasarNET`[9] (Busca & Balland 2018), a neural network-based QSO classifier that updates the spectype and redshift of missed high confidence QSOs, and the Mg II afterburner, which is an emission-based code that updates the spectype of a classified GALAXY to QSO if there is significant broad Mg II emission present in the spectrum (see section 6.2 in Chaussidon et al. 2023). We refer to the combination of these three tools as the 'modified pipeline'.

On the basis of visual inspection (VI), the modified pipeline achieves a good redshift ($\Delta v < 3000\,\mathrm{km\,s^{-1}}$)[10] and spectral type purity of 99 and 94 per cent, respectively for the main QSO survey (see tables 8 and 9 in Alexander et al. 2023). However, from a VI categorization of QSOs with incorrect redshifts and/or incorrect spectypes from the modified pipeline, Alexander et al. (2023) showed that many were found to either have (1) a very red continuum, (2) strong host-galaxy features, or (3) strong broad absorption features.[11] Therefore, our DESI SP sample, the majority of which have very red optical colours (Fig. 2) in addition to pushing to fainter magnitudes than the main DESI QSO selection ($r < 23$ mag), is likely to result in the sort of objects that the DESI pipeline struggles to classify. Due to this, we undertook complete VI of our SP sample of 3038 objects in order to retrieve accurate redshifts and spectypes. Our VI approach is based on that described in section 2.2 of Alexander et al. (2023) and is summarized below.

Each of the 3038 objects in the SP sample are evaluated using the `Prospect`[12] visualization tool; for a detailed description of the `Prospect` tool, see Lan et al. (2023). `Prospect` displays the unsmoothed spectrum, along with the noise spectrum and an indication of where the three arms of the DESI spectrograph overlap. Available tools on the page allow the user to smooth the spectrum and display common absorption and emission lines. The nine best-fitting `redrock` template solutions are also displayed and the best four solutions are available to overlay on the spectrum. The visual assessor is then able to manually (1) adjust and correct the redshift, (2) correct the spectype, (3) add a specific comment, (4) flag any bad data, and (5) assess the quality of the spectrum. Examples of specific comments that were added include flagging Type 2 AGN, BALQSOs, and spectra that included two sources (i.e. those with two redshift solutions). A quality class (VI_quality) of 0 to 4 is provided by the visual assessor for each spectrum, where 0 is the worst quality and 4 is the best quality (the specific meaning of each VI_quality is detailed in Alexander et al. 2023). Every spectrum is visually assessed by two visual assessors and then the files are merged by a VI lead (D. M. Alexander for this data set), who reassesses spectra with significant disagreements between the two assessors and then decides on the final classification and/or redshift.[13] The resulting spectrum is considered 'high quality' with a robust redshift and spectype if the average VI quality class is ≥2.5 (i.e. the lowest quality spectra that are included in our high-quality sample are those where one assessor assigns a quality flag of 2 and the other assigns a 3).

From visually inspecting our DESI SP sample, we found that ∼89 per cent (2700/3038) of the DESI spectra have high quality (VI quality ≥ 2.5) redshifts and spectypes. Out of these high-quality objects, we found that ∼1.6 per cent (42/2700) had two redshift solutions; inspecting the images confirmed that there were indeed two objects within the same fibre, and we therefore removed these objects from our analyses. Excluding the low-quality sources and systems with two objects in the same spectrum, we found that ∼70 per cent (1852/2658) of our SP sample are confirmed as Type 1 QSOs, displaying clear broad emission lines in their optical spectra; this is consistent with the expected fraction of high-quality QSOs from the main survey QSO targets (∼76 per cent; see fig. 4 in Alexander et al. 2023). Additionally, ∼11 per cent (209/1852) of the QSOs were flagged as BALQSOs, displaying broad absorption blueward of C IV (e.g. Petley et al. 2022). We also found that ∼11 per cent (302/2658) of the high-quality spectra are Type 2 AGN, displaying strong [Ne V]λλ3346,3426 but no broad lines, ∼13 per cent (345/2658) are

[8] https://github.com/desihub/redrock
[9] https://github.com/ngbusca/QuasarNET
[10] $\Delta v < 3000\,\mathrm{km\,s^{-1}}$ is equivalent to a $\Delta z = |z_{\mathrm{VI}} - z_{\mathrm{pipeline}}|/(1 + z_{\mathrm{VI}}) < 0.01$, where z_{VI} is the redshift defined from visual inspection.
[11] It is worth noting that improved QSO `redrock` templates are currently being developed. For more details, see Brodzeller et al. (2023).
[12] https://github.com/desihub/prospect
[13] Significant disagreements include assigning different spectypes, redshifts that differ by $>3000\,\mathrm{km\,s^{-1}}$, and quality flags that differ by >1. The majority of disagreements arise for the faintest magnitude sources that are often considered low quality, and therefore are not included in our final sample.

Table 1. Table displaying the percentage and number of high-quality (VI quality ≥ 2.5) objects in our DESI SP sample, in addition to removing systems with two objects in the same spectra, that were classified as QSO (Type 1 and 2), GALAXY, or STAR from the VI. Overall, we find ∼70 per cent of the high-quality sources are Type 1 QSOs, which is consistent with the fraction found from the main DESI QSO selection (see fig. 4 in Alexander et al. 2023).

Spectral type	Percentage of high-quality sources
QSO (Type 1)	69.7 per cent (1852/2658)
QSO (Type 2)	11.4 per cent (302/2658)
GALAXY	13.0 per cent (345/2658)
STAR	6.0 per cent (159/2658)

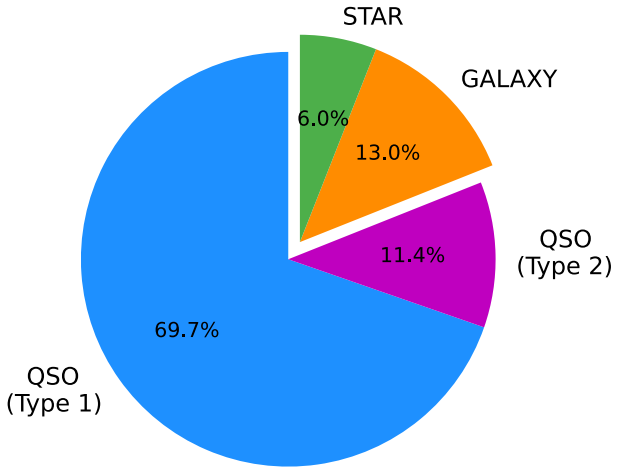

Figure 3. Pie chart showing the fraction of high-quality (VI quality ≥ 2.5) QSO (Type 1 and 2), STAR, and GALAXY spectral classifications from the VI of our DESI SP sample. The number of high-quality objects for each spectype in our SP sample is displayed in Table 1.

galaxies (Fig. B1), and ∼6 per cent (159/2658) are stars (Fig. B2), consistent with the main DESI QSO survey (Alexander et al. 2023); see Table 1 and Fig. 3. This demonstrates that the Mateos et al. (2012) AGN wedge is efficient at selecting QSOs and that our programme is indeed targeting additional QSOs beyond the main DESI survey, rather than introducing a large number of non-QSO contaminants.

Fig. 2 displays the optical colour–colour distribution for the different spectral classes within our secondary sample.[14] We find that ∼87, ∼84, and ∼81 per cent of the QSOs, galaxies, and stars have red optical colours (g–$r > 1.3$ mag or r–$z > 1.1$ mag), respectively. The number of sources for each spectype identified from our VI is displayed in Table 1. For a detailed comparison of the performance of the modified pipeline compared to the VI results, see Appendix A. In this paper, we focus on the QSOs in our sample (Fig. 4); for more discussion on the galaxies and stars within our DESI SP sample, see Appendix B.

3 DATA AND METHODS

In this section, we compare the properties of the QSOs selected by our secondary programme to those selected by the nominal DESI QSO programmes (Section 3.1), our spectral stacking method (Section 3.2), our dust fitting method (Section 3.3), the radio data utilized in this paper (Section 3.4), and the construction of the combined QSO sample used for the main analyses in this paper (Section 3.5).

[14]Note: 66 systems were removed due to imaging issues (e.g. image artefacts, multiple objects in the same fibre, bright nearby stars, edge effects) that resulted in poor photometry in one of the bands, and therefore unrealistic colours.

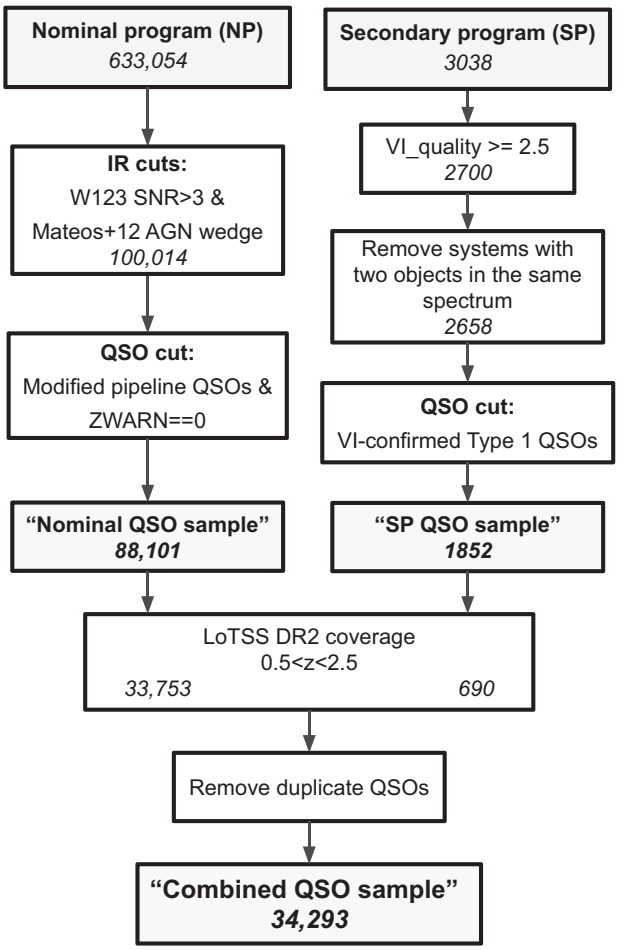

Figure 4. Flow chart illustrating the selection process for the combined QSO sample. We restricted the SP sample (see Fig. 1 for sample selection) to high-quality (VI_quality ≥ 2.5; see Section 2.2) objects and removed systems with two objects in the same spectrum (i.e. two redshift solutions). We then selected the visually confirmed QSOs, resulting in 1852 'SP QSOs'. We selected objects that were targeted by the nominal QSO programme and then applied the same IR cuts used in our SP sample selection. We then selected QSOs based on the spectype from the modified pipeline and also applied a ZWARN cut to ensure the redshifts were robust. The resulting 'nominal QSO sample' consists of 88 101 QSOs. Restricting both samples to the LoTSS DR2 coverage and a redshift range of $0.5 < z < 2.5$, we then combined both QSO sub-samples, resulting in 34 293 QSOs that form the 'combined QSO sample'. An electronic table containing the DESI `TARGETID` for the full combined QSO sample, and additionally the RA, Dec., redshift, spectype, $L_{6\,\mu m}$, and $L_{144\,MHz}$ for the combined QSO sample included in the DESI Early Data Release (DESI Collaboration et al. 2023), is available online.

3.1 How does our SP extend the nominal DESI QSO selection?

For the analyses in this paper, we focus on the broad line QSOs in our SP sample (excluding the 306 Type 2 AGN; see Table 1). We also require a comparison QSO sample in order to assess how our SP sample extends the nominal DESI QSO population. We refer to the

QSOs from the nominal DESI QSO population as 'nominal QSOs' and the QSOs from our SP as 'SP QSOs'. Our selection process for the nominal and SP QSO samples is displayed in Fig. 4, which we describe below.

To construct the nominal QSO sample, we first selected objects that were targeted by the nominal DESI QSO programme (bitmask = QSO). We then applied the same MIR cuts that were used to form our SP sample [Section 2.1; SNR > 3 in the *W*123 bands and satisfying the Mateos et al. (2012) AGN wedge; see Fig. 5]. Finally, we restricted the selection to objects that were classified as QSOs by the modified pipeline and apply ZWARN == 0 to ensure the redshifts are robust. The resulting nominal QSO sample consists of 88 101 QSOs. To construct the SP QSO sample, we selected the visually confirmed QSOs from our SP sample (Section 2.2) which had a VI_quality ≥ 2.5 (i.e. had a robust spectype and redshift) and additionally removed the Type 2 AGN (no broad lines present) and systems with two objects in the same spectrum; this resulted in 1852 QSOs in our SP QSO sample

Due to re-observations, many DESI targets will obtain multiple spectra. In these cases, for our analyses, we use spectra that coadd all observations of a given target. In addition to this, since the DESI SV observations each have distinct target selections (for more details see Myers et al. 2023) there may be multiple coadded spectra across the different campaigns. In these cases, we use the coadded spectrum with the highest squared template signal-to-noise ratio (TSNR2) value. The calculation of the TSNR2 value is target-class dependent, and so in this work, we use the TSNR2_QSO statistic. For more details on the TSNR2 metric, see Guy et al. (2023).

Fig. 5 displays the optical colour–colour distribution for both the nominal and SP QSO samples. We find that, as expected, the majority of the nominal QSO sample, the majority of which lie inside the main colour space used to select DESI QSOs, with only ∼3 per cent (2367/88 101) of QSOs that lie outside; these QSOs were likely selected by the Random Forest QSO selection. Our SP QSO sample expands the colour parameter space of DESI QSOs, with the majority of additional QSOs displaying very red optical colours. It is worth noting that ∼40 per cent (745/1852) of the SP QSOs were also targeted by the nominal QSO programme; these 745 QSOs met both our DESI SP selection criteria and one of the nominal QSO selections. Our DESI SP therefore provides ∼32 per cent more QSOs that lie outside the main region of colour space, i.e. 1107 SP QSOs solely targeted by our programme compared to the 2367 nominal QSOs that fall outside the main colour region (see Fig. 5), despite being only ∼2 per cent the size of the nominal QSO sample.

To understand how the 1852 DESI SP QSOs compare to the SDSS QSOs utilized in our previous studies, we first restricted the SP QSO sample to the SDSS footprint, reducing the sample to 1312 QSOs. We then matched to the DR16 QSO catalogue (Lyke et al. 2020) using a 1 arcsec search radius; this resulted in 107 matches. Therefore, only 8 per cent (107/1312) of the SP QSO sample within the SDSS footprint have also been observed by SDSS and met the criteria used by Lyke et al. (2020) to be included in the SDSS DR16 QSO catalogue. Out of the 107 sources, we found seven with a redshift disagreement between our VI and the SDSS DR16 QSO catalogue; additional VI of these objects clarified that the SDSS redshifts were significantly incorrect. Matching the DR16 QSO catalogue with the other high-quality sources from our SP sample, we found three matches; one was classified as a galaxy and two were classified as Type 2 AGN by our VI. We further investigate these disagreements in Appendix C.

Fig. 6 displays the $L_{6\,\mu m}$ and *r*-band magnitude versus redshift distributions for the nominal and SP QSO samples. To compute the

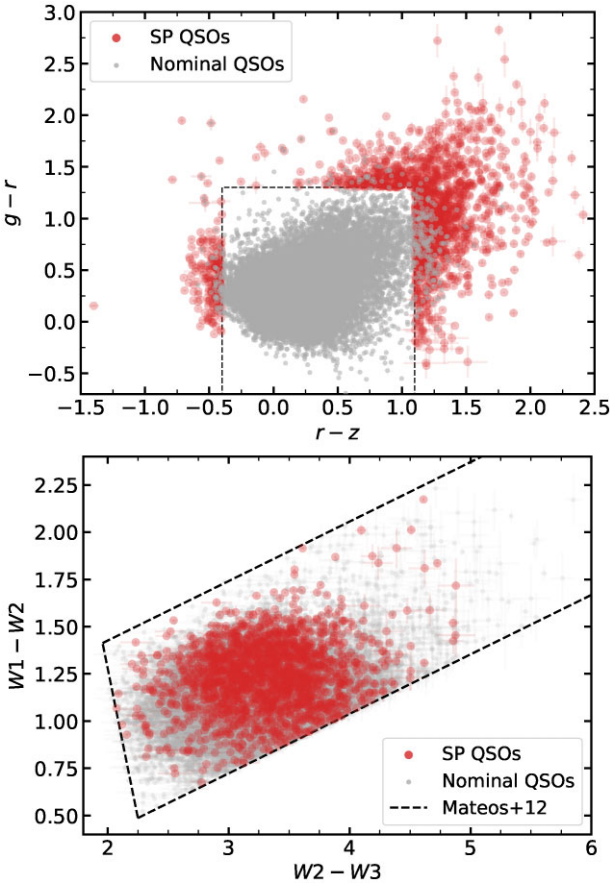

Figure 5. (Top) similar to Fig. 2, but now displaying the SP (red) and nominal (grey) QSO samples (see Fig. 4). Only ∼3 per cent (2367/88 101) of the nominal QSO sample lie outside the colour region indicated by the dashed lines; these QSOs were likely selected by the Random Forest QSO selection. Our SP QSO sample provides 1107 additional unique (i.e. solely targeted by our programme) QSOs to the nominal DESI QSO survey, the majority of which display very red colours (i.e. large *g*–*r* and/or *r*–*z* colours). (Bottom) *WISE* *W*1–*W*2 versus *W*2–*W*3 for the SP (red) and nominal (grey) QSO samples.

$L_{6\,\mu m}$, we used a log-linear interpolation or extrapolation of the fluxes in the *W2* and *W3* bands, following the approach from Klindt et al. (2019). The larger density of SP QSOs at $r \lesssim 22.5$ mag is a result of the different target prioritization during SV3 (see Section 2.1); SP sources *that were also primary targets*, i.e. QSOs (Chaussidon et al. 2023), LRGs (Zhou et al. 2023), or Emission Line Galaxies (ELGs; Raichoor et al. 2023), will have had a far higher probability of being observed than SP targets that were *not* also primary targets. The selection of these primary targets impose brighter magnitude limits than that of our SP, and therefore the targets observed during SV3 are more likely to reside at these brighter magnitudes. The SP QSOs that were also observed by SDSS are shown by the blue diamonds. The highest redshift QSO in the SP and nominal samples are at $z = 4.4$ and 4.6, respectively. On average, the SP QSOs are ∼1.7 mag optically fainter than the QSOs in the nominal sample, demonstrating that our programme is pushing to QSOs with fainter magnitudes. Applying the two-sided Kolmogorov–Smirnov (K–S) test to the redshift and $L_{6\,\mu m}$ distributions of the nominal and SP QSO samples, we cannot rule out that the two samples are drawn from the same parent distribution at a <1 per cent significance level. This also demonstrates that QSOs with fainter optical magnitudes

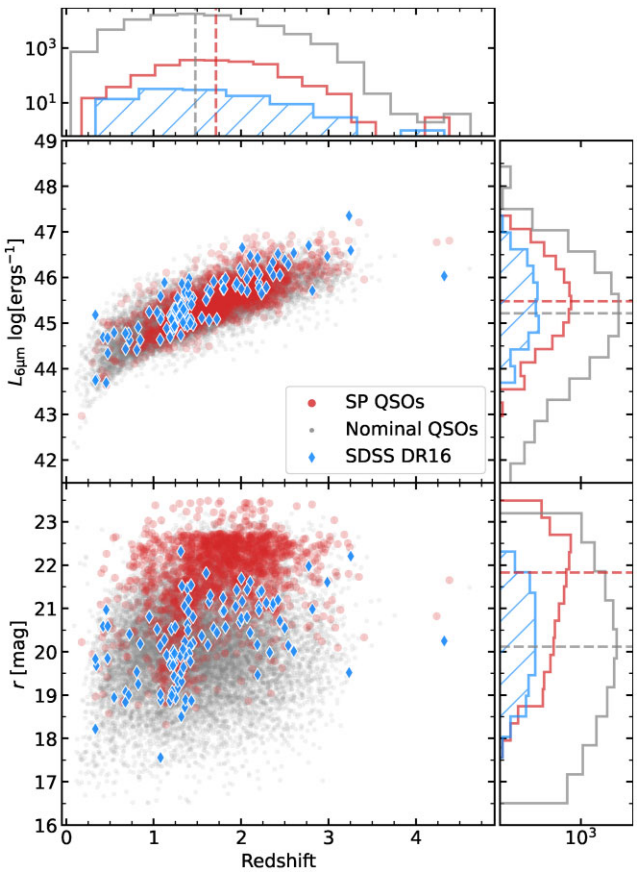

Figure 6. $L_{6\,\mu m}$ (top) and *r*-band magnitude (bottom) versus redshift for the nominal QSO (grey dots) and SP QSO (red circles) samples. The median values for the DESI nominal and SP QSO samples are shown by the dashed lines in the adjacent histograms. The 107 SP QSOs that are also identified in the SDSS DR16 QSO catalogue are highlighted by the blue diamonds.

are not necessarily intrinsically fainter; their optical emission may be relatively fainter due to dust extinction (see Section 4.1). We utilize $L_{6\,\mu m}$ as a tracer for the intrinsic QSO luminosity in Section 4.2.

3.2 Composite construction

To characterize the basic spectral properties of our QSO samples, we constructed composite spectra following the approach outlined in Fawcett et al. (2022); hereafter, F22. First, we trim the ends of the spectrum from each spectral arm to remove noisy data. We then correct for Galactic extinction, using the Schlegel, Finkbeiner & Davis (1998) map and the Fitzpatrick (1999) Milky Way extinction law, and shift to rest-frame wavelengths using the VI redshifts for the SP QSO sample and the redshifts obtained from the modified pipeline for the nominal QSO sample. Each spectrum is then rebinned to a common wavelength grid with 1 Å per bin and normalized to 4500 Å. We then take the median composite, applying a minimum threshold of 30 spectra per bin.

3.3 Dust extinction fitting method

To quantify the amount of extinction present in each QSO, we fitted a blue QSO spectral template with varying amounts of dust extinction to the QSO spectra following the same method as F22. We briefly outline the approach here.

For our blue QSO template, we used the VLT/X-shooter control QSO composite from F22. This composite was constructed by taking the geometric mean of 28 blue QSOs at $1.45 < z < 1.65$ (spanning rest-frame wavelengths $1250 < \lambda < 9000$ Å) observed with X-shooter (Programme ID 0101.B-0739; PI: Klindt). We chose to use this composite rather than constructing a blue composite from DESI spectra due to the broad wavelength coverage of X-shooter; to achieve a similar wavelength range with DESI, we would need to use objects at different redshifts which could result in a non-physical continuum shape (see appendix D in F22 for more discussion). We then masked the emission-line regions and smoothed the spectrum of the blue QSO X-shooter composite with a Gaussian filter ($\sigma = 3$). We fitted this unreddened template to the QSO spectra using a least-squares minimization code, which varied the normalization (avoiding emission-line regions) and $E(B-V)$ parameter [ranging from $-1.0 < E(B-V) < 2.5$ mag[15]], using a simple power-law (PL; $A_V \propto \lambda^{-1}$, $R_V = 4.0$; Fawcett et al. 2022) dust extinction curve which was found to describe the dust in dust-reddened QSOs more effectively than the commonly used Small Magellanic Cloud (SMC; Prevot et al. 1984) extinction law (Fawcett et al. 2022).[16] The measured $E(B-V)$ was allowed to be negative to account for the fact that the X-shooter blue QSO composite used for the fitting will contain a small amount of dust and therefore some DESI QSOs will be bluer than the composite. However, QSOs with negative $E(B-V)$ values should be interpreted with caution; they represent the natural spread in the power-law slope for unobscured QSOs (e.g. Richards et al. 2003), but do not have any physical interpretation.

In order to determine the quality of the fits, we calculated the mean absolute deviation (MAD $= \frac{1}{n}\sum|X-\mu|$; where n is the sample size, X is difference between the model and data, and μ is the mean of the difference). For this work, we choose a conservative cut of MAD $< 4 \times 10^{-5}$ to define whether a fit is good or not. Although this will cut down our sample substantially, it should ensure the results in this paper are robust (see Appendix D for a comparison of how different MAD cuts affect our results).

It has previously been noted that QSOs with low luminosities ($\log L_{6\mu m} \lesssim 45\,\mathrm{erg\,s^{-1}}$) and redshifts ($z \lesssim 1$) can have a substantial contribution of light from the host galaxy (Shen et al. 2011; Calistro Rivera et al. 2021; Fawcett 2022). Therefore, for the QSOs at $z \leq 1$, we first fitted and subtracted a host-galaxy model from the spectrum to avoid potential stellar emission biasing dust extinction estimates towards the QSO. To fit the host-galaxy component, we used the publicly available code `PyQSOFit`[17], following the approach taken in F22. For each source, we first smoothed the spectra with a 10-pixel boxcar and then globally fitted both the continuum and emission lines of the entire spectrum. To fit the continuum, we used a power law, Balmer continuum (BC), third-order polynomial, Fe II continuum, and host-galaxy components. Following the same approach as F22, we chose to apply the Verner et al. (2009) Fe II template for $\lambda > 2000$ Å (obtained via private communication), combined with the Vestergaard & Wilkes (2001) template for $\lambda < 2000$ Å(available on https://github.com/legolason/PyQSOFit/blob/master/pyqsofit/fe_uv.txt), to give a continuous template from 1000–12000 Å. The host galaxy

[15]We note that, even given the natural spread in the power-law slopes for unobscured QSOs, a QSO with an $E(B-V) = -1$ mag is physically impossible. We chose this lower limit to reduce boundary effects in the dust extinction fitting code. For the analyses in this paper, we apply at $E(B-V) > -0.1$ mag cut to esnure we only use reliable fits.
[16]The X-shooter composites and a movie describing our basic fitting approach can be found online: https://github.com/VFawcett/XshooterComposites
[17]https://github.com/legolason/PyQSOFit

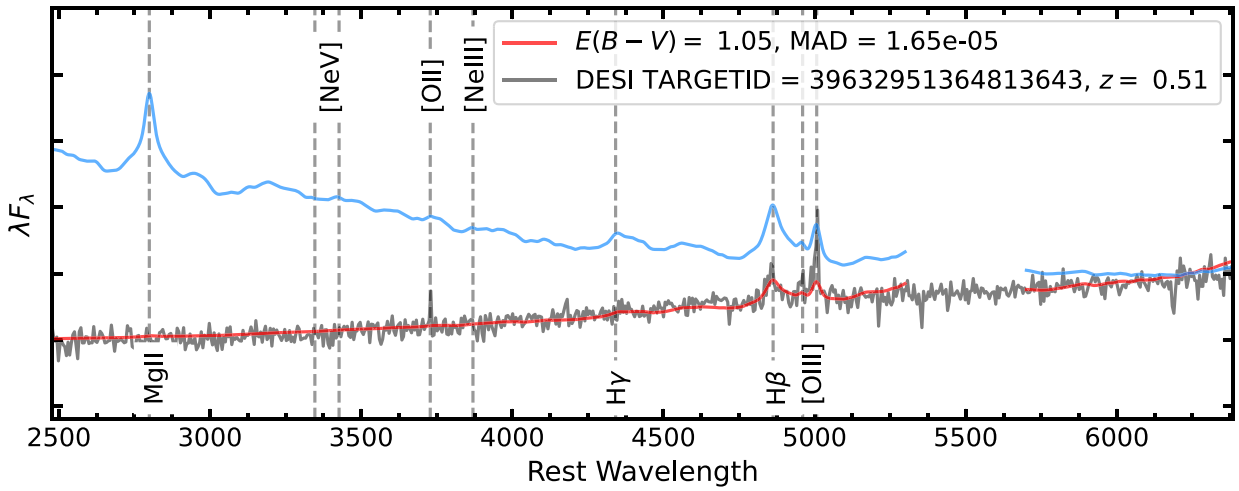

Figure 7. An example of a good dust extinction fit, based on the method described in Section 3.3, for a high $E(B-V)$ QSO. The blue QSO composite (from F22) before and after applying extinction is displayed by the blue and red lines, respectively. The DESI QSO spectrum is displayed by the grey line. The gap in the blue composite between $\lambda \sim 5300$–5700 Å is due to the removal of strong telluric features (see F22 for more details). Additional examples of dust extinction fits, including QSOs with poor fits, can be found in the online supplementary material.

and QSO contributions are decomposed using principal component analysis (PCA; Yip et al. 2004a, b). The PCA method is based on the assumption that the observed QSO spectrum is a combination of two independent sets of eigenspectra taken from pure galaxy and pure QSO samples. We used 5 galaxy and 20 QSO PCA components (following a similar approach as Rakshit, Stalin & Kotilainen 2020), and adopted the stellar host model from Bruzual & Charlot (2003). We used this model instead of the default Yip et al. (2004a) model in `PyQSOFit` due to the wider wavelength coverage. A host-galaxy component is only included if >100 pixels in the host-galaxy template are non-negative; we note the lower resolution of the Bruzual & Charlot (2003) compared to the Yip et al. (2004a) template at higher redshifts may lead to fewer spectra successfully fitted by a host-galaxy template. Overall, we found that ∼10 per cent (97/948) of the SP QSO sample at $z \leq 1$ could successfully be fit with a host-galaxy component. Each of the other continuum components is described in detail in F22. For examples of our dust fitting method, see Fig. 7.

Due to the limited wavelength range of our chosen blue composite ($1250 < \lambda < 9000$ Å), our dust extinction fitting method is less effective for sources at $z > 2.5$ since this corresponds to a large portion of the DESI spectrum with rest-frame wavelengths <1250 Å. The fitting procedure is most effective at $z < 2.0$, where the whole DESI wavelength range is covered by the composite. However, to maximize the source statistics for our dust extinction analyses, we include QSOs at $2.0 < z < 2.5$ that have good fits.

3.4 Radio data

In this work, we utilize radio data from the LOFAR Two Metre Sky Survey (LoTSS) Data Release 2 (LDR2; Shimwell et al. 2022).[18] This survey covers 5740 square deg at 144 MHz, with a median sensitivity of 83 μJy beam^{-1} and 6 arcsec resolution. LDR2 contains 4496 228 sources with a $> 5\sigma$ detection. At equivalent frequencies, for sources with typical synchrotron spectra, LDR2 is ∼9 times deeper than the Faint Images of the Radio Sky at Twenty-centimeters (FIRST; Becker et al. 1995) 1.4 GHz survey; this makes LDR2 ideal to analyse the radio properties of DESI QSOs, which can have modest AGN luminosities.

To determine whether a QSO is 'radio-quiet' or 'radio-loud', we adopted the same 'radio-loudness' parameter ($\mathcal{R}$) as that first used in Klindt et al. (2019), and adapted for 144 MHz data in Rosario et al. (2020), defined as the dimensionless quantity

$$\mathcal{R} = \log_{10} \frac{L_{144\,MHz}}{L_{6\,\mu m}}. \quad (1)$$

The $L_{144\,\mathrm{MHz}}$ is calculated using the methodology described in Alexander et al. (2003), assuming a uniform radio spectral index of $\alpha = 0.7$ for the K-correction. We used the rest-frame 6 μm luminosity to define radio loudness, rather than optical luminosity which is used in most classical definitions (e.g. Kellermann et al. 1989), since L_6 μm is less sensitive to extinction. For example, even at the most extreme $E(B-V)$ for an optically selected QSO [$E(B-V) = 1$ mag] at $z = 1.5$, the difference in L_6 μm due to loss of flux by dust extinction at rest-frame 6 μm is ∼0.15 dex. We scaled the radio-loud/radio-quiet threshold from 1.4 GHz ($\mathcal{R} = -4.2$) to our 144 MHz data by assuming a canonical spectral index of $\alpha = 0.7$ ($S_\nu \propto \nu^{-\alpha}$).[19] This corresponded to a boundary at $\mathcal{R} = -4.5$, which is broadly consistent with the classical radio-quiet/radio-loud threshold (often defined using a 5 GHz-to-2500 Å flux ratio; Kellermann et al. 1989), but is less susceptible to obscuration from dust (see Klindt et al. 2019 for full details).

3.5 Constructing the combined QSO sample

For the scientific analyses in this paper, we constructed a combined QSO sample, which included both our SP and nominal QSO samples

[18] https://lofar-surveys.org/surveys.html

[19] It should be noted that there will be large uncertainties on the radio spectral slope; for example, flatter spectral indices have been found for fainter QSOs (e.g. Gloudemans et al. 2021). The value of $\alpha = 0.7$ was chosen based on the average 144 MHz–1.4 GHz radio spectral index found for SDSS QSOs in Rosario et al. (2020).

in order to maximize the source statistics. We first restricted our nominal and SP QSO samples to the LDR2 survey area using the Multi-Order Coverage map (MOC) provided on the LOFAR website.[20] We then restricted the sample to redshifts $0.5 < z < 2.5$; the lower bound is to ensure minimal contamination from the host galaxy and the upper bound is due to a limitation with our dust fitting method (see Section 3.3). This resulted in 690 and 33 753 QSOs in the SP and nominal samples, respectively. We then matched to the LDR2, adopting a 5 arcsec search radius which resulted in ∼19 per cent (6389/33 753) and ∼31 per cent (216/690) radio-detected QSOs in the nominal and SP samples, respectively (we further explore the radio detection fractions in Section 4.2). Finally, we combined both the restricted nominal and SP QSO samples (removing duplicate QSOs that belong to both samples), resulting in our 'combined QSO sample' which consists of 34 293 QSOs (see Fig. 4).

To estimate the fraction of false matches and objects missed due to radio emission extended beyond 5 arcsec, we utilized the LoTSS DR1 radio catalogue (LDR1; Shimwell et al. 2017), with optical counterparts from Williams et al. (2019).[21] The catalogue from Williams et al. (2019) was created using a combination of likelihood-ratio matching and visual identification, resulting in optical and/or IR counterparts for ∼73 per cent of the LDR1 radio sources. For our false matching estimate, we will use the optical/IR positions of the LDR1 sources as the 'true' positions. Restricting the nominal QSO sample to the much smaller region of LDR1 reduced the sample to only 3057 sources. Adopting the same 5 arcsec search radius as for LDR2, we matched this reduced sample to the radio positions in LDR1, resulting in 645 matches. We then repeated the matching, but instead adopting a 0.″75 search radius (following Rosario et al. 2020) and matching to the positions of the optical counterparts from the value-added catalogue, resulting in 648 matches which represent our 'truth' sample. From this, we were able to determine an estimate for the fraction of false matches by exploring how many of the 645 radio matches within 5 arcsec were not also included in our truth sample; from this, we found a false match fraction of ∼1 per cent (8/645). Similarly, we were able to determine the fraction of missed matches by exploring how many of the truth sample were not included in the sample of 645; from this, we found that ∼2 per cent (11/645) of sources are missed, most likely due to radio emission extended beyond 5 arcsec. Although the false match fraction calculated here is greater than that found for FIRST (using a 10 arcsec matching radius: ∼0.2 per cent; Klindt et al. 2019), which is at a comparable resolution to LoTSS (FIRST: 5 arcsec; LoTSS: 6 arcsec), the sensitivity of LoTSS is ∼9 times deeper than FIRST at equivalent frequencies, assuming a spectral index of $\alpha = 0.7$. We would therefore expect a higher false match fraction from LoTSS due to the higher density of faint sources within a given region. Additionally, our current estimations are limited by source statistics. Our future DESI papers will benefit from the upcoming optical and IR cross-matched LDR2 catalogue for more accurate cross-matching and also a larger DESI SP QSO sample.

4 RESULTS

Our results are based on the combined QSO sample (see Fig. 4) that includes QSOs selected from our secondary target programme (Section 2.1) and QSOs that were targeted by the nominal DESI QSO programme, restricted to the LoTSS DR2 coverage area (to assess radio detection fractions). In the following sections, we explore the line-of-sight dust extinction towards the QSOs (Section 4.1) and the radio properties of the QSOs as a function of dust extinction (Section 4.2).

4.1 Quantifying the line-of-sight dust extinction

Under the assumption that dust is the main cause of reddening in reddened QSOs, we quantified the amount of dust extinction along the line of sight by fitting the spectra of the combined QSO sample with a dust-reddened VLT/X-shooter blue QSO composite (see Section 3.3).

Overall, 58 per cent (20 031/34 293) of the combined QSO sample spectra are well fitted (MAD $< 4 \times 10^{-5}$; see Section 3.3) by the dust-reddened composite. Fig. 7 displays the best-fitting solution for one of the most extreme cases, with a measured $E(B-V) = 1.05$ mag ($A_V \sim 4$ mag); for this source the Mg II emission line is completely obscured, although broad Hβ is still present indicating that it is a QSO. Inspecting the QSOs that are not well fit with a dust extinction curve, we found that they tend to have bluer optical colours (median g–r = 0.26 and 0.21 mag for the QSOs with good and bad fits, respectively), fainter optical magnitudes (median $r = 20.0$ and 20.6 mag, for the QSOs with good and bad fits, respectively), display strong absorption features, and/or reside at higher redshifts (median redshift =1.22 and 1.83 for the QSOs with good and bad fits, respectively); as expected based on the lower effectiveness of our fitting procedure at $z > 2$ due to the limited wavelength range of our chosen blue composite (see Section 3.3). We therefore expect the QSOs with good fits to be slightly biased towards either the more luminous QSOs and/or those with higher dust extinctions. Additionally, from visually assessing the bluest QSOs [$E(B-V) < -0.1$ mag] with an MAD $< 4 \times 10^{-5}$, we found the fits to be unreliable (i.e. the extinction of the QSO compared to the blue composite appears to be consistent with zero, but the measured $E(B-V)$ is clearly underestimated), again highlighting the limitation of our fitting towards blue QSOs. However, due to the significant sample size of the bluest QSOs, we expect this to have little effect on our results (see Appendix D). For the following analyses, we restrict to QSOs with good dust extinction fits and also with a measured $E(B-V) > -0.1$ mag. Examples of QSOs with good and bad dust extinction fits can be found in the online supplementary material.

Fig. 8 displays the distribution of dust-extinction values for the combined QSO sample. The 107 SP QSOs that were additionally identified in the SDSS are also highlighted. This demonstrates that DESI will not only accumulate a more statistically significant sample of reddened QSOs but also extends to QSOs with dust extinctions beyond those observed by the SDSS. Fig. 9 displays the g–r versus r– z optical colour–colour space, with the colourbar representing the measured $E(B-V)$. We find that both the g–r and r–z colour scale with $E(B-V)$, demonstrating that optical colour is a good proxy for dust reddening. In order to maximize the highest $E(B-V)$ end of the QSO population, future QSO selections can utilize this correlation between optical colour and dust extinction in order to select the reddest QSOs.

Overall, DESI can identify QSOs with dust extinctions up to $E(B-V) \sim 1.0$ mag ($A_V \sim 4$ mag; see Fig. 7 for an example fit), comparable to the much smaller sample of NIR-selected heavily reddened QSOs from Banerji et al. (2015). This demonstrates the capability of DESI to help bridge the gap between mildly obscured SDSS red QSOs (e.g. Richards et al. 2003; Klindt et al. 2019; Fawcett et al. 2022), IR-selected red QSOs (e.g. Banerji et al. 2015; Glikman et al. 2015,

[20] https://lofar-surveys.org/dr2_release.html

[21] At the time of writing, the optical and IR identification catalogue for LDR2 has not yet been publicly released.

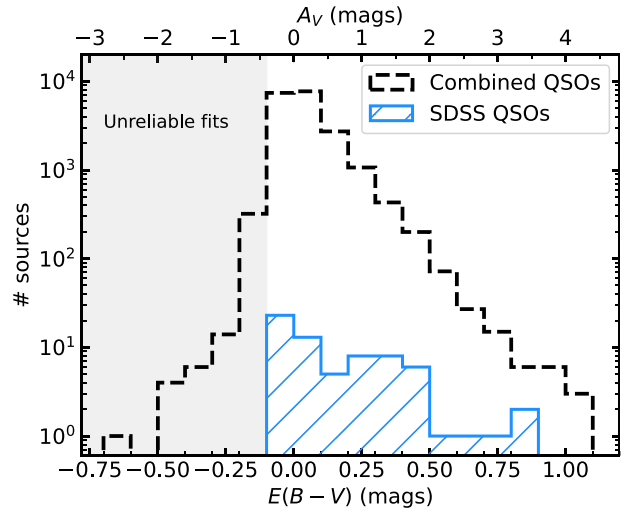

Figure 8. $E(B-V)$ distribution for the combined QSO sample (black dashed line) and SP QSOs that are were also observed by SDSS (hatched blue region), restricted to the sources with good $E(B-V)$ fits. With DESI, we can now observe QSOs with dust extinction values up to $E(B-V) \sim 1$ ($A_V \sim 4$).

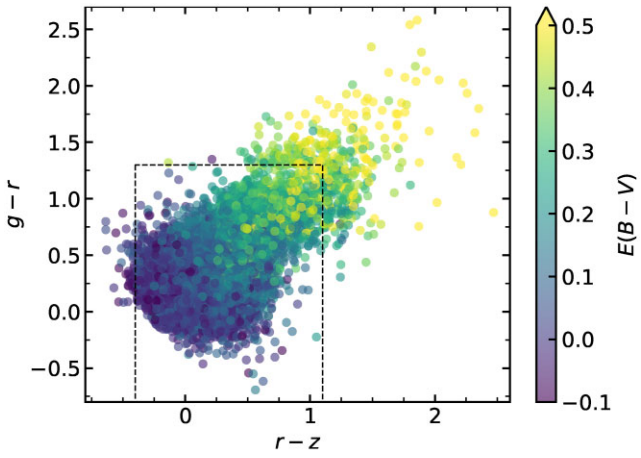

Figure 9. g–r versus r–z for the combined QSO sample, restricted to the QSOs with good $E(B-V)$ fits. The colourbar displays the measured $E(B-V)$ which scales with both g–r and r–z colour. The dashed lines represent the optical colour selection applied in our SP. This demonstrates that optical colour, and our SP, is an effective way of selecting dust-reddened QSOs.

2022), and heavily obscured QSOs (e.g. Andonie et al. 2022). See Section 5.1 for a more detailed comparison with previous red QSO studies. The measured $E(B-V)$ values for the combined QSOs included in the DESI EDR can be found in the electronic table online.

4.2 Exploring the radio properties of dusty QSOs

In our previous work, we identified fundamental differences in the radio properties of red QSOs compared to typical blue QSOs based on the shallower SDSS QSO samples (Klindt et al. 2019; Fawcett et al. 2020, 2021; Rosario et al. 2020). In this paper, we utilize the combined QSO sample, our spectral fitting results, and LDR2 (see Sections 3.4 and 3.5) in order to explore the radio detection fraction as a function of reddening and extend our previous radio results to more heavily reddened QSOs.

In Fig. 10, we show the LDR2 radio detection fraction for the combined QSO sample in bins of $E(B-V)$. On the basis of this figure, it is clear that there is a strong positive correlation between the line-of-sight dust extinction and the radio detection fraction for DESI QSOs. This is consistent with our previous work in which we found that red QSOs in SDSS, selected by their g–i optical colour, have a higher radio detection fraction compared to typical blue QSOs (Klindt et al. 2019; Fawcett et al. 2020, 2021; Rosario et al. 2020). To test that there are no redshift or luminosity biases that are driving this result, we matched the QSOs within each $E(B-V)$ bin in redshift and $L_{6\,\mu m}$ (using a tolerance of 0.05 and 0.2 dex for redshift and $L_{6\,\mu m}$, respectively), using a 2:1 match ratio for the bluest bins to maximize source statistics. We show the LDR2 detection fraction for each matched bin in Fig. 10 by the grey shaded region; although limited on source statistics, a strong positive trend is clearly still present, even when accounting for redshift and luminosity biases (see Appendix D for additional tests). The number of QSOs and associated radio detection fractions for the full and $L_{6\,\mu m}$ – redshift matched samples can be found in Table 2. It is also worth noting that no radio pre-selection is incorporated in the DESI QSO target selection, in comparison to SDSS where some QSOs are selected based on a FIRST radio detection (our previous work addressed this pre-selection; see section 2.2.1 in Klindt et al. 2019). This result therefore corroborates our previous SDSS red QSO results, but utilizing a cleaner, less biased sample and expanding to QSOs with even higher line-of-sight dust extinction (SDSS red QSOs span the range $0.03 \lesssim E(B-V) \lesssim 0.3$; Richards et al. 2003; Klindt et al. 2019; Fawcett et al. 2020; Calistro Rivera et al. 2021).

To give some basic insight on the radio properties, in Fig. 11, we show the $L_{6\,\mu m}$ versus $L_{144\,MHz}$ distribution for the radio-detected combined QSO sample in three bins of $E(B-V)$, with the radio-loud/radio-quiet threshold displayed by the dashed red line (see Section 3.4); we find that 93 per cent of the radio-detected QSOs in the combined sample are radio-quiet. Assuming a 5σ upper limit for the LDR2 undetected QSOs (415 μJy), we estimate a radio-quiet fraction for the overall combined QSO sample of ∼99 per cent. Therefore, the trend in radio detection fraction found in Fig. 10 is driven by radio-quiet QSOs, consistent with our previous work. We do not find a significant difference in the median radio-loudness across increasing $E(B-V)$ bins [$\mathcal{R} \sim -5.9$ for each $E(B-V)$ bin]. However, we do find a decrease in the number of radio-loud QSOs with increasing $E(B-V)$ (∼8, 5, and 3 per cent with increasing $E(B-V)$ bin); we explore this result more in Section 5.2.

5 DISCUSSION

We have presented the first results from our ongoing secondary target programme in DESI that uses an optical and MIR colour selection to expand the optical colour space probed by the nominal DESI QSO selection. Our programme complements the QSOs from the nominal DESI QSO selections, which are predominantly blue, and pushes to higher extinctions than those selected by both the SDSS and DESI QSO samples. Combining the QSOs from our secondary target programme and the nominal DESI QSOs, the key result in this paper is the striking positive relationship between amount of line-of-sight dust extinction and the radio detection fraction for QSOs (Fig. 10). This clearly demonstrates that the presence of dust (and/or gas, i.e. opacity) is an important factor for the production of radio emission in radio-quiet QSOs. In the following sections, we discuss how these results complement and extend the previous red QSO studies, including the overlap between our sample and Extremely Red Quasars (ERQs; e.g. Hamann et al. 2017; Section 5.1), and

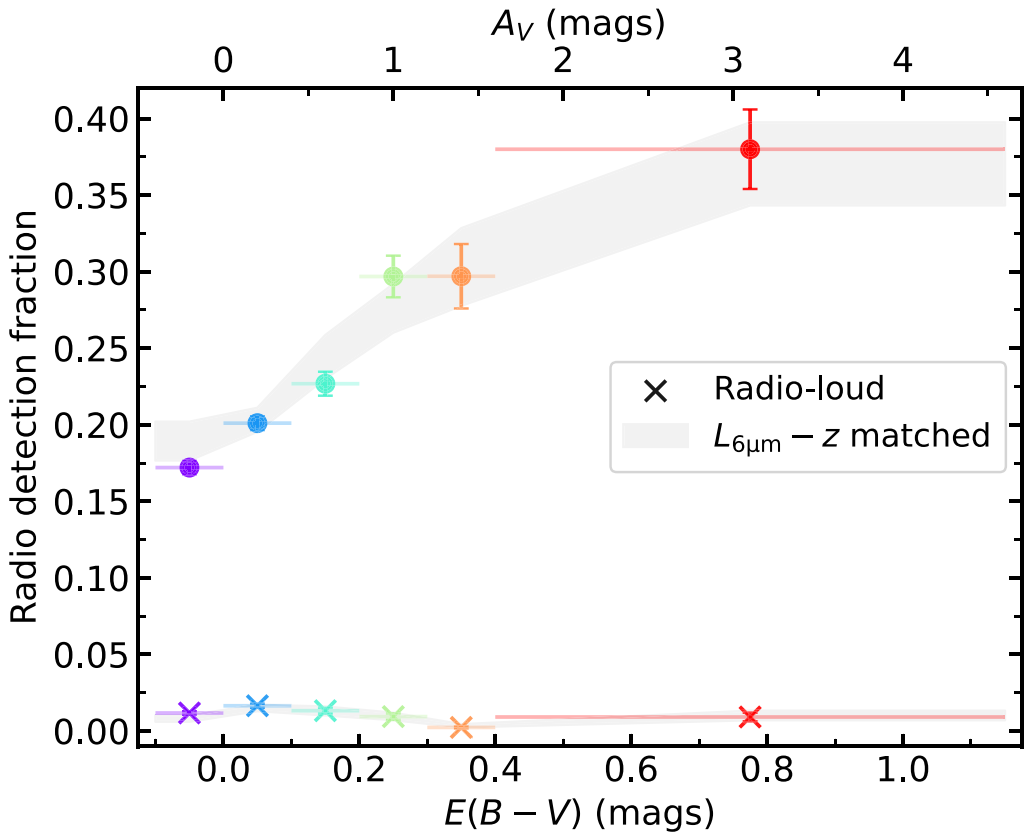

Figure 10. LDR2 radio-detection fraction and radio-loud ($\mathcal{R} \geq -4.5$) fraction for the combined QSO sample in bins of $E(B-V)$ [the fraction is calculated relative to the number of combined QSOs per $E(B-V)$ bin], calculated using a PL extinction curve (see Section 3.3). The grey shaded region displays the $L_{6\mu m}$–z matched bins. The error bars were calculated using the method described in Cameron (2011) and corresponds to 1σ binomial uncertainties. There is a positive correlation between radio detection fraction and $E(B-V)$, even when accounting for any redshift or luminosity biases, demonstrating a striking relationship between the radio emission and the line-of-sight dust extinction towards QSOs. We find that the radio-loud fraction is $\lesssim$2 per cent across all $E(B-V)$ bins, suggesting the correlation between radio-detection fraction and dust extinction is not due to large scale/high-luminosity radio jets. There is a small decrease in the radio-loud fraction out to $E(B-V) \sim 0.4$ mag. The number of QSOs and associated radio detection and radio loud fractions can be found in Table 2.

Table 2. Table displaying the number of QSOs, radio-detection fraction, and radio-loud ($\mathcal{R} \geq -4.5$) fraction in each $E(B-V)$ bin from Fig. 10, for the full combined QSO sample and the $L_{6\mu m}$–z matched sample.

$E(B-V)$	Combined QSO sample (all)			Combined QSO sample ($L_{6\,\mu m}$–z matched)		
	# QSOs	Radio-detection frac. (#)	Radio-loud frac. (#)	# QSOs	Radio-detection frac. (#)	Radio-loud frac. (#)
−0.1–0.0	7412	17.2 % (1275)	1.2 % (87)	861	18.9 % (163)	0.8 % (7)
0.0–0.1	7720	20.1 % (1552)	1.6 % (127)	2529	20.3 % (514)	1.5 % (38)
0.1–0.2	2725	22.7 % (618)	1.3 % (36)	843	24.4 % (206)	1.3 % (11)
0.2–0.3	1068	29.7 % (317)	0.9 % (10)	739	27.6 % (204)	0.9 % (7)
0.3–0.4	431	29.7 % (128)	0.2 % (1)	297	30.3 % (90)	0.3 % (1)
0.4–1.1	329	38.0 % (125)	0.9 % (3)	297	37.0 % (110)	1.0 % (3)

explore the origin of the radio emission in radio-quiet dusty QSOs (Section 5.2).

5.1 A comparison to previous red and obscured QSO studies

5.1.1 SDSS red QSOs

In our previous work, exploring SDSS selected red and blue QSOs, we found that the majority of the red QSOs were red due to modest amounts of dust extinction ($E(B-V) \lesssim 0.2$ mag; Calistro Rivera et al. 2021; F22). For example, utilizing VLT/X-shooter data, F22 found that the red QSO spectra displayed the characteristic frequency dependent spectral turnover at UV – optical wavelengths, indicating they were red due to line-of-sight dust extinction. To illustrate the improvements in the selection of dust-reddened QSOs by our DESI programme, in Fig. 12 we show a comparison between the X-shooter red and blue composites from F22 and our combined DESI sample, in similar luminosity–redshift matched bins of measured $E(B-V)$ as in Fig. 10 (see Section 3.3). First, we confirm that the DESI composites appear more dust reddened (i.e. a stronger UV spectral turnover) with increasing $E(B-V)$, providing confidence in our dust extinction fitting method. We also find that the reddest DESI composite has

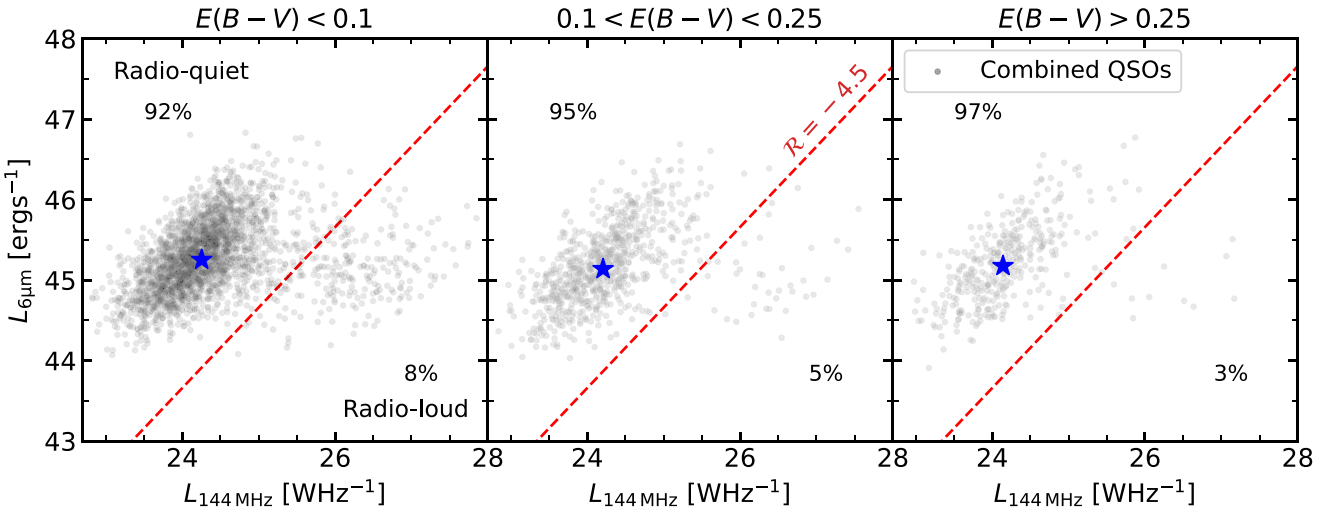

Figure 11. $L_{6\,\mu m}$ versus $L_{144\,MHz}$ for the radio-detected combined QSO sample (see Section 4.1) in three bins of $E(B-V)$. The division between radio-loud and radio-quiet sources is displayed by the dashed red line ($\mathcal{R} = -4.5$; see Section 3.4); ∼93 per cent of the radio-detected combined QSO sample are radio-quiet (this increases to ∼99 per cent when taking the radio-undetected QSOs into account, which are radio-quiet based on a 5σ LDR2 upper limit). The blue stars indicate the median value in each $E(B-V)$ bin; there is no significant change in median radio-loudness across the $E(B-V)$ bins for the combined QSO sample. However, we do find a significant change in the fraction of radio-detected QSOs that are radio-loud ($\mathcal{R} \geq -4.5$) across the $E(B-V)$ bins (indicated on the plot), with fewer radio-loud QSOs at higher $E(B-V)$ values; we further investigate this result in Section 5.2.

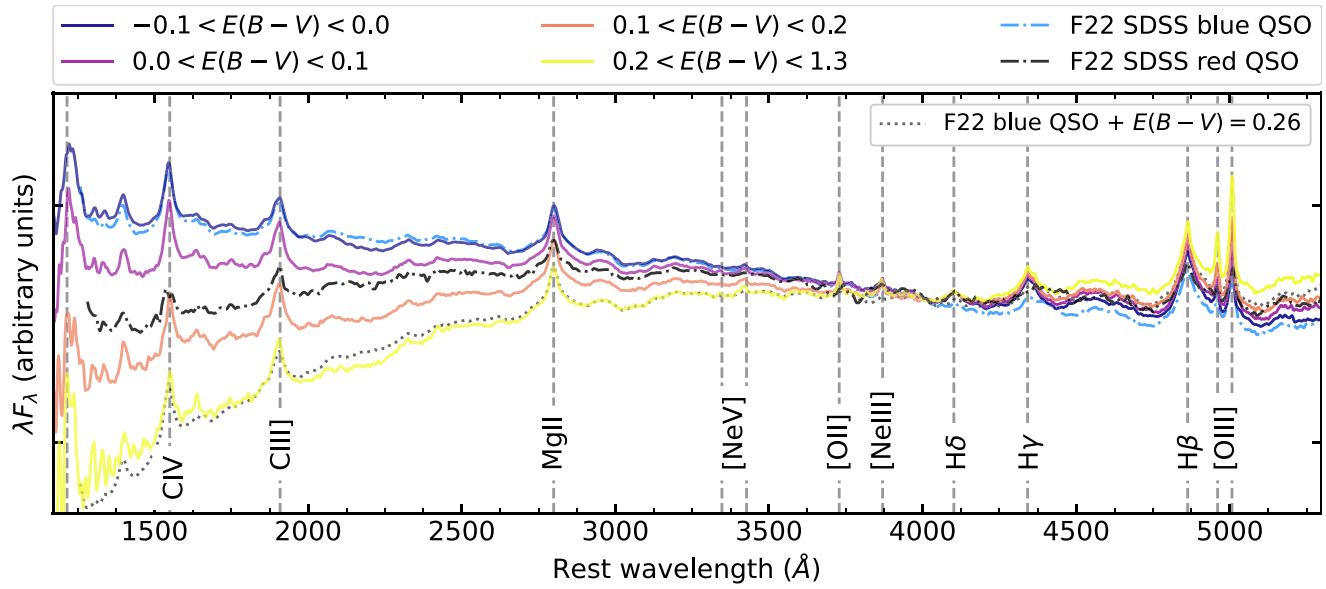

Figure 12. Comparison of composite spectra, normalized at 4000 Å, for the combined DESI QSO sample in luminosity–redshift matched bins of $E(B-V)$ (solid lines) to the *X-shooter* red and blue composites from F22 (dot-dashed black and blue lines, respectively). The F22 blue composite with the average dust extinction for the reddest DESI bin applied is displayed by the dotted line; this agrees very well with the reddest DESI composite. We find that the DESI composites appear to be more dust reddened with increasing $E(B-V)$, and that the reddest composite has over twice the amount of average dust extinction as that of the F22 red composite. This again demonstrates that our DESI SP will obtain a statistically significant sample of heavily reddened QSOs that are not observed by SDSS.

over ∼0.15 mag more dust extinction on average compared to the F22 SDSS red composite, again demonstrating that with DESI we can obtain a statistically significant sample of luminous heavily reddened QSOs that are missed by the optically shallow SDSS survey.

We have also previously found that SDSS red QSOs display enhanced radio emission compared to typical blue QSOs (Klindt et al. 2019; Fawcett et al. 2020, 2021; Rosario et al. 2020). Similarly, Glikman et al. (2022) used a *WISE*–2MASS colour selection to define a sample of red QSOs with dust extinctions $E(B-V) > 0.25$ mag ($A_V \gtrsim 0.8$ mag; by this definition, the SDSS QSOs defined as 'red' in our previous work would be classified as 'blue' in the Glikman et al. (2022) sample) and found a higher radio detection fraction for their more heavily reddened red QSOs compared to their blue sample (see fig. 18 therein), using both FIRST and VLASS. These results are in agreement with Fig. 10, where we have now extended to more

Table 3. Comparison of previous red QSO selections and their corresponding range in $E(B-V)$: the QSOs explored in this study, SDSS red QSOs (Klindt et al. 2019; Fawcett et al. 2020; Rosario et al. 2020; Calistro Rivera et al. 2021, F22), IR-selected red QSOs (Glikman et al. 2018), *WISE*-2MASS (W2M) red QSOs (Glikman et al. 2022), heavily reddened QSOs (HRQs) (Banerji et al. 2015), extremely red quasars (ERQs) (Ross et al. 2015; Hamann et al. 2017), obscured QSOs and unobscured IR-selected red QSOs (Andonie et al. 2022). For a more comprehensive comparison of red and obscured QSOs, see table 2.1 within Klindt (2022).

Sample name	Key selection	$E(B-V)$ [mag]	# sources	Reference
DESI combined QSOs	DESI QSO selections & Mateos et al. (2012) *W*123	0.1–1.1	4553	This work
		0.25–1.1	1177	This work
SDSS red QSOs	DR7 (*g*–*i*) 90th percentile	$\lesssim$0.2	4899	Klindt et al. (2019)
	DR14 (*g*–*i*) 90th percentile		21 800	Fawcett et al. (2020)
WISE red QSOs	$W1-W2>0.7$ & $W2-W3>2$ & $W3-W4>1.9$ & $E(B-V)>0.25$	0.25–1.2	21	Glikman et al. (2018)
W2M red QSOs	$0.5<W1-W2<2$ & $2<W2-W3<4.5$ & $E(B-V)>0.25$	0.25–1.2	63	Glikman et al. (2022)
HRQs	$J-K>1.6$ & $W1-W2>0.85$	0.5–1.5	38	Banerji et al. (2015)
ERQs	$i-W3>4.6$	$\lesssim$0.7	97	Hamann et al. (2017)
Obscured	SED fitting	$\gtrsim$2	355	Andonie et al. (2022)
IR red QSOs		0.05–1	223	Andonie et al. (2022)

extreme red QSOs, which suggests that the radio enhancement in red QSOs is linked to a higher amount of line-of-sight dust extinction. Table 3 displays the number of combined QSOs with SDSS-like reddening [$E(B-V)>0.1$ mag] and the number that satisfy the Glikman et al. (2022) red QSO cut [$E(B-V)>0.25$ mag], resulting in 4533 and 1177 red QSOs, respectively. This demonstrates that the DESI survey will obtain a statistically significant sample of heavily reddened QSOs.

5.1.2 *Obscured QSOs*

Extending our previous red QSO work to fully obscured QSOs (e.g. Compton thick), Andonie et al. (2022) compared the VLA 1.4 and 3 GHz radio properties of a sample of obscured and unobscured QSOs in the COSMOS field (by their definition, even our extreme DESI red QSOs are unobscured) and found that the obscured QSOs have higher radio detection fractions compared to unobscured QSOs (see fig. 14 therein). However, interestingly, they found that the obscured QSOs have consistent radio detection fractions to red QSOs. This could suggest that either (1) there is a 'saturation' point in Fig. 10, whereby increasing the amount of line-of-sight dust extinction towards a QSO will *not* result in a higher radio detection fraction, (2) the origin of the radio emission is different in obscured and unobscured QSOs, or (3) the differences in the radio detection fraction are more modest at the higher sensitivity radio data in COSMOS. Utilizing the increased source statistics in future DESI data releases, we can populate the highest $E(B-V)$ end of Fig. 10, testing whether the radio detection fraction increases or does indeed start to plateau, as would be the case in the former scenario; by the end of the five-year survey, we expect to add additional bins at $E(B-V)>0.4$ in Fig. 10.

5.1.3 *Extremely red QSOs*

Since our DESI study pushes to more reddened QSOs than the previous SDSS red QSO studies, it is interesting to investigate the overlap between our DESI red QSOs and the population of extremely red quasars (ERQs; see Table 3 for a comparison of the red QSO selections discussed in this section), which are selected based on their optical–MIR colours, as compared to the pure optical or NIR selection approach often used to select red QSOs (Ross et al. 2015; Hamann et al. 2017). ERQs have been found to host some of the most powerful outflows identified in QSOs (e.g. Zakamska et al. 2016; Perrotta et al. 2019; Lau et al. 2022), and therefore have also been suggested as a candidate transitional population in the evolution of QSOs (see discussion in Section 5.2). However, due to the depth of SDSS, previous studies have only analysed a small sample of the most luminous ERQs. In order to assess the capability of DESI (in particular, our SP) at selecting ERQs, we first defined an ERQ selection based on the optical–MIR colours of the SDSS ERQ sample from Hamann et al. (2017). Hamann et al. (2017) defined an ERQ to have redshifts >2.0, *W*3 SNR > 3, and $i-W3\geq 4.6$ mag. For our ERQ classification, we based our selection on the full Hamann et al. (2017) ERQ sample that meet the $i-W3\geq 4.6$ mag selection; 141 objects. Since the DR9 photometry does not include an *i*-band magnitude, we defined our DESI ERQ selection based on the $z-W3$ colours, qualitatively consistent with the ERQ selection of Ross et al. (2015) and Hamann et al. (2017); we classify a QSO as an ERQ if it has an optical–MIR colour that satisfies $z-W3>3.9$ mag. This resulted in ∼39 per cent (714/1852) of our SP QSO sample classified as ERQs, in comparison to only ∼7 per cent (6167/88 101) for the nominal QSO sample, demonstrating that our SP is also efficient at selecting ERQs; in future data releases, we will build up a statistically significant sample of these rare systems. Our future papers will explore the dust extinction, emission-line, and radio properties of DESI ERQs and how they compare to the general red QSO population.

5.1.4 *Mg II absorption line systems*

A number of studies have noted that a larger fraction of reddened QSOs host narrow absorption lines compared to typical blue QSOs (Richards et al. 2003; Chen et al. 2020; Fawcett et al. 2022). The strongest and most distinctive of these absorption lines is the Mg II λλ 2796, 2803 doublet, with a laboratory separation between the two lines of 7.1772 Å (Pickering, Thorne & Webb 1998). Mg II absorption that is close to the Mg II emission line (i.e. where $z_{\rm abs}\sim z_{\rm em}$) is thought to be associated with the host galaxy of the QSO, whereas blueshifted absorption (i.e. where $z_{\rm abs}<<z_{\rm em}$) is thought to be due to an intervening system. Previous studies have found that QSOs that host associated absorption lines (AALs) are, on average, redder, with stronger [O II] emission, and are more likely to be radio detected, compared to both QSOs with intervening absorption lines and QSOs with no absorbers (Vanden Berk et al. 2008; Shen & Ménard 2012; Khare et al.

2014; Chen et al. 2020). The strength of the Mg II absorption in systems with AALs has also been found to correlate with the dust extinction and radio properties, suggesting an intrinsic nature for the AALs (Vanden Berk et al. 2008; Chen et al. 2020). Despite the similarities in radio properties between QSOs with AALs and red QSOs, the measured dust extinctions are far more modest in the AAL QSOs, with an $E(B-V) \sim 0.03$–0.06 mag (Chen et al. 2020). Furthermore, Shen & Ménard (2012) suggested that AAL QSOs may be a transitional population between heavily reddened QSOs and typical blue QSOs. In order to assess whether AAL QSOs are driving the relationship between reddening and the radio detection fraction found in Fig. 10 and our previous SDSS work (Klindt et al. 2019; Fawcett et al. 2020; Rosario et al. 2020), we explored the properties of QSOs with Mg II absorbers in our DESI combined QSO sample, utilizing the catalogue from Napolitano et al. (2023).

Napolitano et al. (2023) used an autonomous spectral pipeline to detect associated or intervening Mg II absorption through an initial line-fitting process and a Markov Chain Monte Carlo (MCMC) sampler. To create the Mg II absorber catalogue, they ran their detection pipeline on 83 207 DESI QSOs at $0.3 < z < 2.5$ which are part of the DESI EDR. They found 20.1 per cent (16 707/83 207) of the unique QSO spectra have Mg II absorbers, with a large number that contain multiple absorption features.

Restricting the combined QSO sample to those included in the EDR significantly reduces the sample to 11 092 QSOs. Matching to the Napolitano et al. (2023), Mg II catalogue resulted in 4924 absorption systems in 30.7 per cent (3400/11 092) unique QSO spectra. Of these, 16.4 per cent (808/4924) are associated, defined by $-6000 < v_{\rm off} < 5000\,{\rm km\,s^{-1}}$ ($v_{\rm off} = c \times \frac{z_{\rm MgII} - z_{\rm QSO}}{1+z_{\rm QSO}}$; Napolitano et al. 2023), and the rest are intervening. Comparing the radio detection fractions, we found 24.3, 13.4, and 13.4 per cent of the AAL QSOs, intervening absorber QSOs, and QSOs without any absorption systems have LDR2 radio detections, respectively. We also found the AAL QSOs are considerably redder than the intervening and no absorber systems, with a median $E(B-V) \sim 0.12$, 0.00, and 0.03 mag for the QSOs with associated, intervening, and no absorbers, respectively). Since the median $E(B-V)$ associated with the absorption feature has been found to be $\lesssim$0.03 mag, this suggests that AALs are more likely to be associated with red QSOs. This is further shown in Fig. 13, which displays the fraction of associated and intervening Mg II absorbers as a function of $E(B-V)$; a larger fraction of associated absorbers are found in QSOs with higher amounts of dust extinction, consistent with previous studies (Shen & Ménard 2012; Chen et al. 2020; Fawcett et al. 2022). This suggests the Mg II absorption is associated with the dust/gas that is also responsible for reddening the spectrum. We found that the fraction of QSOs with intervening absorbers decreases with increasing $E(B-V)$; by definition, intervening absorbers will fall at the bluer end of the spectrum (relative to Mg II), which will have a lower signal to noise for red QSOs due to dust extinction, and so this could reduce the effectiveness of the automated pipeline at detecting absorption features.

Fig. 13 also displays the radio-detection fraction for the sample with and without both the intervening and associated absorber systems. We find that removing the absorber systems has little effect on the overall trend with $E(B-V)$, which is consistent with Fig. 10 albeit with lower source statistics, suggesting that the amount of dust (and/or gas, i.e. opacity) in a QSO is the most important factor for determining whether a QSO is radio detected or not. However, since QSOs with more dust are more likely to host an AAL, QSO samples selected purely on the presence of Mg II AALs are likely to be redder and more radio-detected compared to QSOs without absorbers.

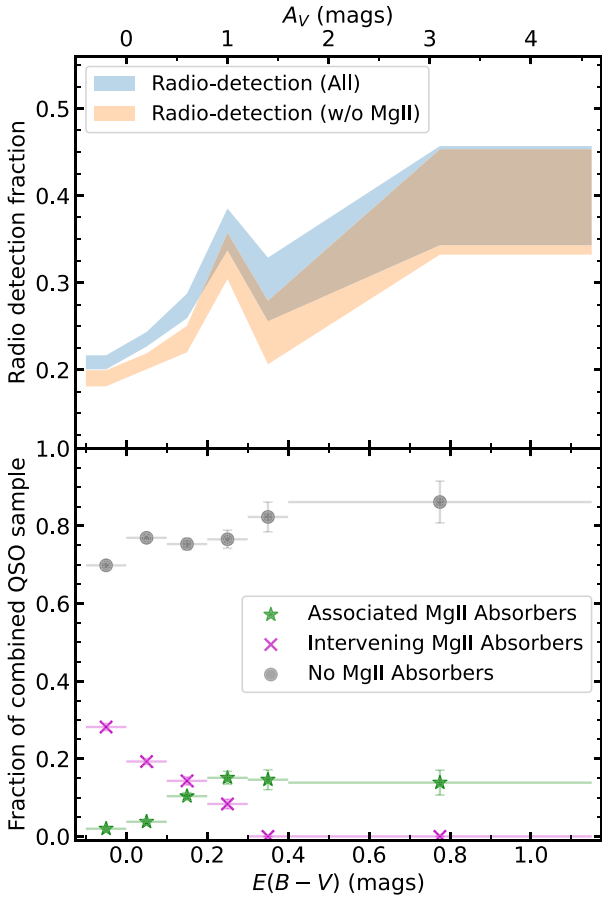

Figure 13. (Top) LDR2 radio-detection fraction including (blue) and excluding (orange) Mg II absorption systems, and (bottom) fraction of Mg II associated absorbers (green stars), intervening absorbers (magenta crosses), and no Mg II absorbers (grey circles) for the combined QSO sample, restricted to systems explored in Napolitano et al. (2023) (those included in the DESI EDR), as a function of $E(B-V)$. Excluding the systems with Mg II absorption present does not affect the overall trend between radio detection fraction and $E(B-V)$. The fraction of QSOs with associated Mg II absorbers increases with increasing $E(B-V)$, which is consistent with previous work that found QSOs with associated Mg II absorption tend to be redder and have higher radio detection fractions compared to both QSOs with intervening absorbers and those without any absorbers. The fraction of intervening Mg II absorbers decreases with increasing $E(B-V)$, which is likely due to the lower signal to noise in the reddest systems which may reduce the effectiveness of the automated spectral pipeline at detecting intervening absorbers.

5.2 Origin of the radio emission in dusty radio-quiet QSOs

The strong relationship between the line-of-sight dust extinction and radio detection fraction displayed in Fig. 10 demonstrates an intrinsic link between dust and the production of radio emission in QSOs. However, it is currently unclear what is the dominant mechanism for the production of the radio emission. Calculating the fraction of radio-loud ($\mathcal{R} > -4.5$; see Section 3.4) QSOs in the combined sample as a function of $E(B-V)$, we find that $\lesssim$2 per cent of the QSOs (both radio-detected and undetected) are radio-loud across all bins (see Fig. 10 and Table 2). This demonstrates that radio-loud

QSOs, typically hosting a large-scale radio jet, are not driving the correlation between dust extinction and radio-detection fraction, in agreement with our previous red QSO studies (Klindt et al. 2019; Fawcett et al. 2020; Rosario et al. 2020).

The low-frequency radio emission probed by LOFAR is dominated by synchrotron emission, which may be produced by star formation, low-powered/frustrated jets, and/or winds causing shocks in a dusty circumnuclear/ISM region (for more details on the production of radio emission in radio-quiet QSOs, see review by Panessa et al. 2019). To perform a detailed analysis into the origin of the radio emission, multifrequency and/or higher spatial resolution radio observations are required; our future radio study utilizing radio data from the upgraded Giant Meter Radio Telescope (uGMRT; PI: V. Fawcett), in addition to high spatial resolution e-MERLIN data (Rosario et al. 2021), aims to do just this. In the following section, we discuss some of the potential scenarios that could be driving the connection between the line-of-sight dust extinction and radio detection fraction in DESI QSOs.

In our previous work exploring the properties of SDSS red QSOs, we found no differences in the star-formation properties between the red and blue QSOs. This was based on deep IR data from the COSMOS region (Fawcett et al. 2020) and composite SEDs (Calistro Rivera et al. 2021). We therefore concluded that the radio emission in SDSS red QSOs was likely driven by AGN processes such as winds or jets. However, given that DESI pushes to redder systems, it is unclear whether this conclusion still holds for our combined QSO sample. In addition to comparing obscured and unobscured QSOs in COSMOS, Andonie et al. (2022) also compared the star-formation properties between a blue [$E(B-V) < 0.05$ mag] and red [$0.05 < E(B-V) < 1.0$ mag] unobscured sub-sample. They found no difference in the star-formation properties between the two samples, despite finding a significantly higher radio-detection fraction for the red QSOs compared to the blue QSOs. Given that the red and blue QSOs from Andonie et al. (2022) cover a similar $E(B-V)$ range to Fig. 10, this suggests that star formation is not a strong driver of the relation between dust extinction and radio detection fraction. Furthermore, Calistro Rivera et al. (in preparation) perform comprehensive SED fitting of red and blue QSOs in the LOFAR deep fields and find no difference in the star-formation properties. However, individual star formation measurements are required to robustly demonstrate this for our sample. Calculating the $L_{144\,\mathrm{MHz}}$ from star-forming galaxies with a star-formation rate of $100\,\mathrm{M_{\odot}\,yr^{-1}}$ (equivalent to local ultraluminous infrared galaxies; ULIRGs), based on the FIR-radio correlation from Calistro Rivera et al. (2017), we find that only ∼16 per cent of the radio-detected QSOs may have a substantial contribution from star formation to the radio emission, ∼83 per cent of which are at $z < 1$. Therefore, the most likely mechanism that links the presence of dust in the QSOs to the radio emission is either frustrated jets and/or winds causing shocks in a dusty circumnuclear/ISM region.

Recent hydrodynamic simulations have predicted that radiation pressure on dust is an effective way to launch outflows (e.g. Costa et al. 2017). The optical and UV radiation from the accretion disc is absorbed and re-emitted by the dust as IR radiation, transferring momentum to the ambient gas (Ishibashi & Fabian 2015; Thompson et al. 2015). These AGN-driven outflows can have high velocities (∼ 1000–3000 $\mathrm{km\,s^{-1}}$), extend up to tens of kpc (Cicone et al. 2015), and are likely launched along the polar axis (e.g. Hönig et al. 2013). When the outflow interacts with the surrounding dense ISM, they can cause shocks which accelerate electrons, producing radio emission (Faucher-Giguère & Quataert 2012; Zubovas & King 2012; Nims, Quataert & Faucher-Giguère 2015). Dusty winds are therefore a promising mechanism for the production of radio emission in radio-quiet red QSOs. This is supported by a number of studies that have observed powerful outflows in red QSOs (Urrutia et al. 2009; Hwang et al. 2018; Perrotta et al. 2019; Calistro Rivera et al. 2021; Vayner et al. 2021; Stacey et al. 2022), although it is not always clear whether this is a result of luminosity biases (e.g. Villar Martín et al. 2020; F22).

On the other hand, low-powered jet-ISM interactions have also been found to be important in radio-quiet QSOs (Jarvis et al. 2019; Girdhar et al. 2022; Murthy et al. 2022; Audibert et al. 2023). For example, jet–ISM simulations have found that an initially collimated radio jet can get spread into lower powered jet filaments, which can potentially drive shocks in the ISM (Wagner & Bicknell 2011; Bicknell et al. 2018). A significant fraction of the jet's energy (up to 30 per cent; Wagner & Bicknell 2011) can be imparted to the surrounding gas clouds, driving outflows. This is in agreement with observational studies that find correlations between the strength and/or spatial location of the ionized outflow with a young or weak radio jet (Cresci et al. 2015, 2023; Morganti et al. 2015; Molyneux, Harrison & Jarvis 2019; Venturi et al. 2021). The connection between these low-powered radio jets and the expanding ionized gas bubbles have been shown to result in both negative and positive feedback in the host galaxy (Gaibler et al. 2012; Jarvis et al. 2019; Girdhar et al. 2022), demonstrating the importance for studying the radio–ISM interactions in these radio-quiet systems.

With our current data, it is difficult to distinguish between the jet versus wind scenarios (or whether it is some combination of both). However, in either case, the resulting effect is a jet/wind shocking the surrounding ISM. This will likely drive out the surrounding gas/dust in a short-lived 'blow-out' phase (e.g. Glikman 2017) that may eventually reveal a typical blue QSO (Hopkins et al. 2006). Therefore, the relationship between dust and radio emission in QSOs may be crucial to our understanding of QSO evolution.

In future DESI papers, we will robustly compare the emission line and radio properties of a statistically significant sample of QSOs as a function of $E(B-V)$, in order to understand to what extent, differences in the observed outflow properties and/or accretion state drive the striking relationship in Fig. 10. In addition to our future DESI studies, we have obtained four-band radio data observed with the uGMRT (PI: V. Fawcett) for a sample of 20 red and 20 blue radio-detected QSOs with high spatial resolution e-MERLIN 1.4 GHz data from Rosario et al. (2021). With these data, we can construct sensitive radio SEDs over 0.12–3 GHz (with the addition of VLASS), in order to search for spectral signatures of radio jets (e.g. Bicknell et al. 2018). For example, if the QSOs are similar to compact steep spectrum (CSS) and gigahertz-peaked spectrum (GPS) sources (see review by O'Dea 1998), which are thought to be jet dominated, then we can expect a spectral turnover in the radio SED around ∼100 MHz and ∼1 GHz (for CSS and GPS sources, respectively). Therefore, we can explore (1) whether the radio SEDs of red and blue QSOs are different, and (2) if jets are the dominant mechanism for producing radio emission in radio-quiet dusty QSOs. Furthermore, future Very Long Baseline Interferometry (VLBI) observations will be crucial to resolve and confirm potential pc-scale radio jet morphologies in these systems.

6 CONCLUSIONS

In this paper, we present the first ∼8 months of our DESI secondary target programme that utilizes a MIR and optical selection to expand the DESI QSO colour space, in particular to reddened QSOs.

Combining our SP QSO sample with the larger nominal DESI QSO sample, we have explored the dust extinction and radio properties. From our analyses, we find that

(i) **Our secondary target programme extends the nominal DESI QSO programme to more extreme optical colours, the majority of which are red**: From visually inspecting the spectra of the 3038 objects from our secondary target programme, we find that ∼89 per cent have high quality spectral and redshift classifications. Of these high quality sources, 81 per cent are QSOs (both Type 1 and Type 2), 13 per cent are galaxies, and 6 per cent are stars (Fig. 3). Overall, our programme provides ∼32 per cent more QSOs that lie outside of the main colour space compared to the nominal QSO sample despite being ∼2 per cent of the size (Fig. 5), and also pushes to fainter optical magnitudes than the nominal QSO programme (Fig. 6). See Sections 2, 3.1, and 5.1.

(ii) **DESI is capable of detecting QSOs with up to $E(B-V)\sim1$ mag of dust extinction:** Measuring the dust extinction by fitting the spectra of the combined QSOs with a dust-reddened blue QSO composite, we find up to ∼1 mag in $E(B-V)$ ($A_V\sim4$ mag; Figs 8), comparable to NIR-selected heavily reddened QSOs. We also find that optical colour strongly correlates with dust extinction, demonstrating that optical colour is an effective way to select dust-reddened QSOs (Fig. 9). Finally, splitting the combined QSO sample into $E(B-V)$ bins, we find that the reddest composite [$E(B-V)>0.2$ mag] has over ∼0.15 mag more dust extinction than the Fawcett et al. (2022) SDSS red QSO composite, again demonstrating that with DESI, we can push to much higher amounts of dust extinction than in SDSS (Fig. 12). See Sections 4.1 and 5.1.

(iii) **There is a strong link between the radio detection fraction and amount of line-of-sight dust extinction in QSOs:** Utilizing the combined QSO sample to maximize the source statistics, we explored the 144 MHz radio properties of the QSOs using the LoTSS DR2 (LDR2) data set. Comparing the LDR2 radio detection fraction of the combined QSO sample as a function of $E(B-V)$, we find a strong positive correlation (Fig. 10), even when accounting for any redshift or luminosity biases, demonstrating that the amount of line-of-sight dust extinction is closely linked to the radio emission in a QSO. We find that $\lesssim$2 per cent of the combined QSO sample are radio-loud (Fig. 11), suggesting that large-scale radio-loud jets are not driving the relation between radio-detection fraction and dust extinction. Therefore, we suggest the origin of this predominantly radio-quiet emission is likely due to frustrated jets or outflows causing shocks in a dust/gas rich ISM, which may drive away the dust in a 'blow-out' phase. See Sections 4.2 and 5.2.

We have demonstrated that DESI will observe a statistically significant sample of dust-reddened QSOs, bridging the gap between the more modest SDSS red QSOs and the heavily reddened NIR-selected QSOs. From our results, we have shown that red QSOs are likely undergoing a dusty blow-out phase, in which winds and/or jets clear out the surrounding dust and gas, eventually revealing a blue typical QSO. Therefore, red QSOs are important objects to study in the context of AGN feedback and QSO evolution. In future papers, we will use our growing DESI sample to investigate whether there are any differences in the outflow properties of QSOs as a function of dust extinction and to explore statistically significant sub-samples of rare/exotic QSOs (e.g. extremely red quasars and low-ionization broad absorption line QSOs).

ACKNOWLEDGEMENTS

We would like to thank the anonymous referee for their constructive comments that greatly helped improve the clarity and structure of the paper.

VAF and CMH acknowledge funding from a United Kingdom Research and Innovation grant (code: MR/V022830/1) and (VAF) previously a quota studentship through grant code ST/S505365/1 funded by the Science and Technology Facility Council. DMA and ACE acknowledges the Science and Technology Facilities Council (through grant code ST/P000541/1). AB supported by the U.S. Department of Energy, Office of Science, Office of High Energy Physics, under Award No. DESC0009959. DR acknowledges the support of STFC grant NU-012097. ADM was supported by the U.S. Department of Energy, Office of Science, Office of High Energy Physics, under Award Number DE-SC0019022. We would like to thank E. Verner for providing us with the Fe II template presented in Verner et al. (2009).

This work uses observations collected at the European Southern Observatory under ESO programme 0101.B-0739(A).

LOFAR data products were provided by the LOFAR Surveys Key Science project (LSKSP; https://lofar-surveys.org/) and were derived from observations with the International LOFAR Telescope (ILT). LOFAR (van Haarlem et al. 2013) is the Low Frequency Array designed and constructed by ASTRON. It has observing, data processing, and data storage facilities in several countries, which are owned by various parties (each with their own funding sources), and which are collectively operated by the ILT foundation under a joint scientific policy. The efforts of the LSKSP have benefited from funding from the European Research Council, NOVA, NWO, CNRS-INSU, the SURF Co-operative, the UK Science and Technology Funding Council and the Jülich Supercomputing Centre.

This material is based upon work supported by the U.S. Department of Energy (DOE), Office of Science, Office of High-Energy Physics, under Contract No. DE–AC02–05CH11231, and by the National Energy Research Scientific Computing Center, a DOE Office of Science User Facility under the same contract. Additional support for DESI was provided by the U.S. National Science Foundation (NSF), Division of Astronomical Sciences under Contract No. AST-0950945 to the NSF's National Optical-Infrared Astronomy Research Laboratory; the Science and Technologies Facilities Council of the United Kingdom; the Gordon and Betty Moore Foundation; the Heising-Simons Foundation; the French Alternative Energies, and Atomic Energy Commission (CEA); the National Council of Science and Technology of Mexico (CONACYT); the Ministry of Science and Innovation of Spain (MICINN), and by the DESI Member Institutions: https://www.desi.lbl.gov/collaborating-institutions. Any opinions, findings, and conclusions or recommendations expressed in this material are those of the author(s) and do not necessarily reflect the views of the U. S. National Science Foundation, the U. S. Department of Energy, or any of the listed funding agencies.

The authors are honoured to be permitted to conduct scientific research on Iolkam Du'ag (Kitt Peak), a mountain with particular significance to the Tohono O'odham Nation.

DATA AVAILABILITY

The SV data and spectra underlying this article are publicly available in the DESI Early Data Release (DESI Collaboration et al. 2023), with the remaining data and spectra obtained from the Main survey publicly available in a future data release (DESI collaboration et al. in preparation).

The radio and VLT/X-shooter data used in this study are publicly available in online archives.

The data underlying the figures in this paper are available online: https://doi.org/10.5281/zenodo.8147342.

Electronic tables containing the DESI `TARGETID` for the full combined QSO and SP samples can be found online. Additional redshift and photometric information are provided for the sources included in the DESI Early Data Release (DESI Collaboration et al. 2023).

REFERENCES

Alexander D. M. et al., 2003, AJ, 125, 383
Alexander D. M. et al., 2023, AJ, 165, 124
Alexander D. M., Hickox R. C., 2012, New Astron. Rev., 56, 93
Andonie C. et al., 2022, MNRAS, 517, 2577
Audibert A. et al., 2023, A&A, 671, L12
Banerji M., Alaghband-Zadeh S., Hewett P. C., McMahon R. G., 2015, MNRAS, 447, 3368
Banerji M., McMahon R. G., Hewett P. C., Alaghband-Zadeh S., Gonzalez-Solares E., Venemans B. P., Hawthorn M. J., 2012, MNRAS, 427, 2275
Becker R. H., White R. L., Helfand D. J., 1995, ApJ, 450, 559
Bicknell G. V., Mukherjee D., Wagner A. Y., Sutherland R. S., Nesvadba N. P. H., 2018, MNRAS, 475, 3493
Brodzeller A. et al., 2023, AJ, 166, 66
Bruzual G., Charlot S., 2003, MNRAS, 344, 1000
Busca N., Balland C., 2018, preprint (arXiv:1808.09955)
Calistro Rivera G. et al., 2017, MNRAS, 469, 3468
Calistro Rivera G. et al., 2021, A&A, 649, A102
Cameron E., 2011, PASA, 28, 128
Cardelli J. A., Clayton G. C., Mathis J. S., 1989, ApJ, 345, 245
Chaussidon E. et al., 2023, ApJ, 944, 107
Chen Z.-F., Qin H.-C., Chen Z.-G., Pang T.-T., Gui R.-J., Yi S.-X., 2020, ApJ, 893, 25
Cicone C. et al., 2015, A&A, 574, A14
Cooper A. P. et al., 2023, ApJ, 947, 37
Costa T., Rosdahl J., Sijacki D., Haehnelt M. G., 2017, MNRAS, 473, 4197
Cresci G. et al., 2015, A&A, 582, A63
Cresci G. et al., 2023, A&A, 672, A128
DESI Collaboration et al., 2016a, preprint (arXiv:1611.00036)
DESI Collaboration et al., 2016b, preprint (arXiv:1611.00037)
DESI Collaboration et al., 2022, AJ, 164, 207
DESI Collaboration et al., 2023, preprint (arXiv:2306.06308)
Dey A. et al., 2019, AJ, 157, 168
Faucher-Giguère C.-A., Quataert E., 2012, MNRAS, 425, 605
Fawcett V. A., 2022, PhD thesis, Durham University, UK, http://etheses.dur.ac.uk/14707/
Fawcett V. A., Alexander D. M., Rosario D. J., Klindt L., 2021, Galaxies, 9, 107
Fawcett V. A., Alexander D. M., Rosario D. J., Klindt L., Fotopoulou S., Lusso E., Morabito L. K., Calistro Rivera G., 2020, MNRAS, 494, 4802
Fawcett V. A., Alexander D. M., Rosario D. J., Klindt L., Lusso E., Morabito L. K., Calistro Rivera G., 2022, MNRAS, 513, 1254
Fitzpatrick E. L., 1999, PASP, 111, 63
Gaibler V., Khochfar S., Krause M., Silk J., 2012, MNRAS, 425, 438
Gentile Fusillo N. P. et al., 2018, MNRAS, 482, 4570
Georgakakis A., Clements D. L., Bendo G., Rowan-Robinson M., Nandra K., Brotherton M. S., 2009, MNRAS, 394, 533
Girdhar A. et al., 2022, MNRAS, 512, 1608
Glikman E. et al., 2012, ApJ, 757, 51
Glikman E. et al., 2018, ApJ, 861, 37
Glikman E. et al., 2022, ApJ, 934, 119
Glikman E., 2017, RNAAS, 1, 48
Glikman E., Gregg M. D., Lacy M., Helfand D. J., Becker R. H., White R. L., 2004, ApJ, 607, 60
Glikman E., Helfand D. J., White R. L., Becker R. H., Gregg M. D., Lacy M., 2007, ApJ, 667, 673
Glikman E., Simmons B., Mailly M., Schawinski K., Urry C. M., Lacy M., 2015, ApJ, 806, 218
Gloudemans A. J. et al., 2021, A&A, 656, A137
Gordon Y. A. et al., 2020, RNAAS, 4, 175
Guy J. et al., 2023, ApJ, 165, 144
Hahn C. et al., 2023, AJ, 165, 253
Hamann F. et al., 2017, MNRAS, 464, 3431
Harrison C. M., Costa T., Tadhunter C. N., Flütsch A., Kakkad D., Perna M., Vietri G., 2018, Nat. Astron., 2, 198
Heckman T. M., Best P. N., 2014, ARA&A, 52, 589
Hönig S. F. et al., 2013, ApJ, 771, 87
Hopkins P. F., Hernquist L., Cox T. J., Di Matteo T., Robertson B., Springel V., 2006, ApJS, 163, 1
Hopkins P. F., Hernquist L., Cox T. J., Kereš D., 2008, ApJS, 175, 356
Hwang H.-C., Zakamska N. L., Alexandroff R. M., Hamann F., Greene J. E., Perrotta S., Richards G. T., 2018, MNRAS, 477, 830
Ishibashi W., Fabian A. C., 2015, MNRAS, 451, 93
Jarvis M. E. et al., 2019, MNRAS, 485, 2710
Kellermann K. I., Sramek R., Schmidt M., Shaffer D. B., Green R., 1989, AJ, 98, 1195
Khare P., Berk Daniel V., Rahmani H., York D. G., 2014, ApJ, 794, 66
Kim D., Im M., 2018, A&A, 610, A31
Klindt L., 2022, PhD thesis, Durham University, UK, http://etheses.dur.ac.uk/14314/
Klindt L., Alexander D. M., Rosario D. J., Lusso E., Fotopoulou S., 2019, MNRAS, 488, 3109
Kormendy J., Ho L. C., 2013, ARA&A, 51, 511
Lan T.-W. et al., 2023, ApJ, 943, 68
Lang D., 2014, AJ, 147, 108
Lau M. W., Hamann F., Gillette J., Perrotta S., Rupke D. S. N., Wylezalek D., Zakamska N. L., 2022, MNRAS, 515, 1624
Lyke B. W. et al., 2020, ApJS, 250, 8
Maddox N., Hewett P. C., Warren S. J., Croom S. M., 2008, MNRAS, 386, 1605
Mainzer A. et al., 2011, ApJ, 731, 53
Mainzer A. et al., 2014, ApJ, 792, 30
Mateos S. et al., 2012, MNRAS, 426, 3271
Mignoli M. et al., 2013, A&A, 556, A29
Molyneux S. J., Harrison C. M., Jarvis M. E., 2019, A&A, 631, A132
Morabito L. K. et al., 2019, A&A, 622, A15
Morganti R., Oosterloo T., Raymond Oonk J. B., Frieswijk W., Tadhunter C., 2015, A&A, 580, A1
Murthy S., Morganti R., Wagner A. Y., Oosterloo T., Guillard P., Mukherjee D., Bicknell G., 2022, Nat. Astron., 6, 488
Myers A. D. et al., 2023, AJ, 165, 50
Napolitano L. et al., 2023, AJ, 166, 99
Nims J., Quataert E., Faucher-Giguère C.-A., 2015, MNRAS, 447, 3612
O'Dea C. P., 1998, PASP, 110, 493
Panessa F., Baldi R. D., Laor A., Padovani P., Behar E., McHardy I., 2019, Nature, 3, 387
Perrotta S., Hamann F., Zakamska N. L., Alexandroff R. M., Rupke D., Wylezalek D., 2019, MNRAS, 488, 4126
Petley J. W. et al., 2022, MNRAS, 515, 5159
Petter G. C. et al., 2022, ApJ, 927, 16
Pickering J. C., Thorne A. P., Webb J. K., 1998, MNRAS, 300, 131
Prevot M. L., Lequeux J., Maurice E., Prevot L., Rocca-Volmerange B., 1984, A&A, 132, 389
Prieto C. A. et al., 2020, RNAAS, 4, 188
Raichoor A. et al., 2020, RNAAS, 4, 180
Raichoor A. et al., 2023, AJ, 165, 126
Rakshit S., Stalin C. S., Kotilainen J., 2020, ApJS, 249, 17
Richards G. T. et al., 2003, AJ, 126, 1131
Rosario D. J., Alexander D. M., Moldon J., Klindt L., Thomson A. P., Morabito L., Fawcett V. A., Harrison C. M., 2021, MNRAS, 505, 5283
Rosario D. J., Fawcett V. A., Klindt L., Alexander D. M., Morabito L. K., Fotopoulou S., Lusso E., Calistro Rivera G., 2020, MNRAS, 494, 3061
Ross N. P. et al., 2015, MNRAS, 453, 3932

Ruiz-Macias O. et al., 2020, RNAAS, 4, 187
Sanders D. B., Soifer B. T., Elias J. H., Madore B. F., Matthews K., Neugebauer G., Scoville N. Z., 1988, ApJ, 325, 74
Schlafly E. F. et al., 2023, preprint (arXiv:2306.06309)
Schlegel D. J., Finkbeiner D. P., Davis M., 1998, ApJ, 500, 525
Shen Y. et al., 2011, ApJS, 194, 45
Shen Y., Ménard B., 2012, ApJ, 748, 131
Shimwell T. W. et al., 2017, A&A, 598, A104
Shimwell T. W. et al., 2022, A&A, 659, A1
Silber J. H. et al., 2023, AJ, 165, 9
Stacey H. R., Costa T., McKean J. P., Sharon C. E., Calistro Rivera G., Glikman E., van der Werf P. P., 2022, MNRAS, 517, 3377
Stern D. et al., 2012, ApJ, 753, 30
Thompson T. A., Fabian A. C., Quataert E., Murray N., 2015, MNRAS, 449, 147
Urrutia T., Becker R. H., White R. L., Glikman E., Lacy M., Hodge J., Gregg M. D., 2009, ApJ, 698, 1095
van Haarlem M. , et al. 2013, A&A, 556, A2
Vanden Berk D. et al., 2008, ApJ, 679, 239
Vayner A. et al., 2021, MNRAS, 504, 4445
Venturi G. et al., 2021, A&A, 648, A17
Verner E., Bruhweiler F., Johansson S., Peterson B., 2009, Phys. Scr, 134, 014006
Vestergaard M., Wilkes B. J., 2001, ApJS, 134, 1
Villar Martín M., Perna M., Humphrey A., Castro Rodríguez N., Binette L., Pérez González P. G., Mateos S., Cabrera Lavers A., 2020, A&A, 634, A116
Wagner A. Y., Bicknell G. V., 2011, ApJ, 728, 29
Weymann R. J., Morris S. L., Foltz C. B., Hewett P. C., 1991, ApJ, 373, 23
White R. L., Helfand D. J., Becker R. H., Gregg M. D., Postman M., Lauer T. R., Oegerle W., 2003, AJ, 126, 706
Williams W. L. et al., 2019, A&A, 622, A2
Wright E. L. et al., 2010, AJ, 140, 1868
Yèche C. et al., 2020, RNAAS, 4, 179
Yip C. W. et al., 2004a, AJ, 128, 585
Yip C. W. et al., 2004b, AJ, 128, 2603
York D. G. et al., 2000, AJ, 120, 1579
Zakamska N. L. et al., 2016, MNRAS, 459, 3144
Zhou R. et al., 2020, RNAAS, 4, 181
Zhou R. et al., 2023, AJ, 165, 58
Zubovas K., King A., 2012, ApJ, 745, L34

SUPPORTING INFORMATION

Supplementary data are available at *MNRAS* online.

Figure S1: Four examples of good (MAD $< 4 \times 10^{-5}$) dust extinction fits, based on the method described in Section 3.3, for increasing $E(B-V)$.
Figure S2: Four examples of bad (MAD $> 4 \times 10^{-5}$) dust extinction fits, based on the method described in Section 3.3, for increasing MAD values.

Please note: Oxford University Press is not responsible for the content or functionality of any supporting materials supplied by the authors. Any queries (other than missing material) should be directed to the corresponding author for the article.

APPENDIX A: TESTING THE PERFORMANCE OF THE MODIFIED PIPELINE

Comparing the redshifts and spectral types ('spectypes') for the DESI SP sample obtained from the VI to the modified pipeline, we found that the modified pipeline correctly identifies ∼71 per cent of all spectypes (see Table A1). We also found that >72 per cent of our sample are high-quality QSOs compared to ∼47 per cent classified by the modified pipeline; this is predominantly due to the number of reddened QSOs in our sample (see Section 2.1 and Alexander et al. 2023) and highlights the necessity of VI to reliably classify red QSOs in our sample.

A comparison between the resulting high-quality VI redshifts and those from the modified pipeline for our DESI SP sample is displayed in Fig. A1. We found ∼66 per cent (1795/2700) of all high-quality objects have correct redshifts ($\Delta z = |z_{\rm VI} - z_{\rm RR}|/(1 + z_{\rm VI}) < 0.01$, which corresponds to a $\Delta v \leq 3000\,{\rm km\,s^{-1}}$) as measured by the modified pipeline. In the SP QSO sample, ∼58 per cent (1076/1852) have correct redshifts from the modified pipeline. Of the other ∼42 per cent, ∼78 per cent were also incorrectly classified as galaxies; these systems are all assigned a redshift <1.7 by the modified pipeline, due to the maximum redshift that the modified pipeline can assign to a galaxy. The fraction of correct redshifts in our SP QSO sample is a lot lower than that found in the VI of the

Table A1. Table displaying the number of high-quality objects (removing the 42 systems with two objects in the same spectrum; see Section 2.2) that were classified as a QSO, GALAXY, or STAR in the modified pipeline compared to the VI classifications; we found that 765 of the visually identified QSOs are missed by the modified pipeline (classified as a GALAXY or STAR). Overall, the modified pipeline correctly identifies ∼71 per cent of spectypes.

		VI			
		QSO	GALAXY	STAR	Total
Modified pipeline	QSO	1389	9	0	1398 (53 %)
	GALAXY	753	336	4	1093 (41 %)
	STAR	12	0	155	167 (6 %)
	Total	2154 (81 %)	345 (13 %)	159 (6 %)	2658

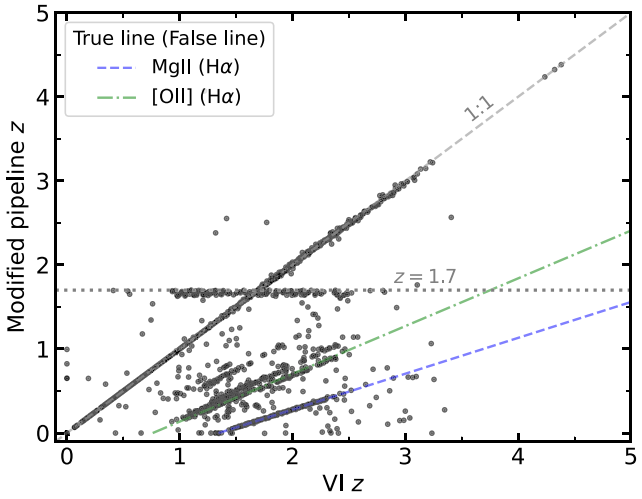

Figure A1. Redshifts obtained from the modified pipeline versus the redshifts obtained from VI (see Section 2.2); we find that ∼66 per cent of the high-quality objects have correct redshifts ($\Delta v \leq 3000\,\mathrm{km\,s^{-1}}$) as measured by the modified pipeline. The green and blue dashed lines highlight two redshift tracks caused by the modified pipeline incorrectly identifying the Mg II emission line as H α and [O II]λ3727, respectively. The dashed grey line represents the 1:1 relation. The horizontal dotted grey line indicates the maximum redshift that the modified pipeline can assign to a galaxy ($z \sim 1.7$; QSOs do not have a redshift restriction in the modified pipeline); the cluster of sources around this line therefore represents QSOs misidentified as galaxies.

nominal DESI QSOs (∼99 per cent); this is again predominantly due to the high number of dust-reddened QSOs in our sample, which are substantially more likely to be miss-classified (Alexander et al. 2023).

APPENDIX B: POPULATION STACKS

Fig. B1 displays the composite of the 358 and 306 high-quality galaxies and Type 2 AGN in our DESI SP sample (see Section 2.1), following the approach outlined in Section 3.2. The Type 2 AGN display strong high ionization line emission lines, including [Ne V]$\lambda\lambda$3346,3426, that implies the presence of hard radiation from an AGN (Mignoli et al. 2013). In the galaxy composite, the emission lines are narrower compared to the Type 2 composite and the [Ne V] lines are faint-to-non-existent, demonstrating little-to-no AGN activity in these objects. For a more detailed discussion of the galaxies in DESI, see Raichoor et al. (2020, 2023), Ruiz-Macias et al. (2020), Zhou et al. (2020, 2023), Hahn et al. (2023). Lan et al. (2023). The broader [O III] in the Type 2 composite compared to the galaxy composite implies that the Type 2 AGN are more likely to host powerful outflows; future work will investigate the emission line properties of our SP sample.

Fig. B2 displays the composite of the 164 high-quality stars in our DESI SP sample, split into 'red' ($r - z > -0.4$) and 'blue' ($r - z < -0.4$). The red stars show strong molecular features that are indicative of late-type cool stars (e.g. M-type), whereas the blue stars are mainly (DA) white dwarfs due to the broad and shallow Balmer features (see fig. 11 in Gentile Fusillo et al. 2018).[22] For a more detailed discussion of the stars in DESI, see Prieto et al. (2020) and Cooper et al. (2023).

[22]For examples of different types of stellar spectra, see http://classic.sdss.org/dr5/algorithms/spectemplates/.

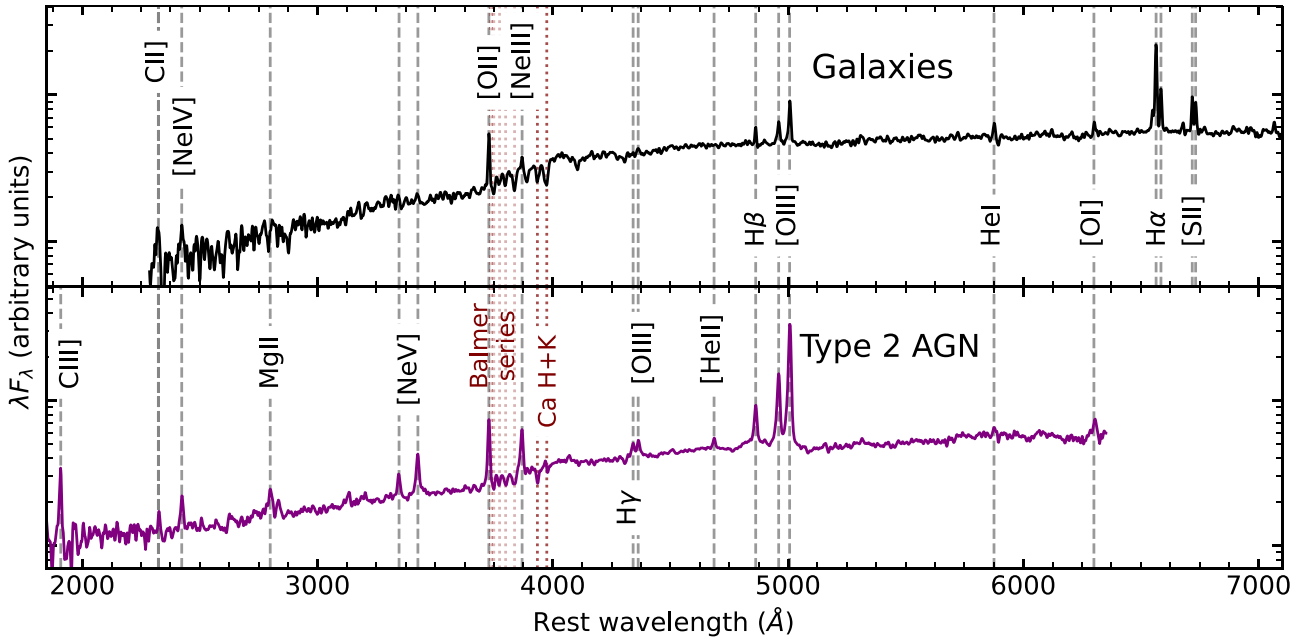

Figure B1. Composite of 358 and 306 high-quality VI-confirmed galaxies (top) and Type 2 AGN (bottom) in our DESI SP sample (see Section 2.1). The main emission and absorption features are indicated; the prominent [Ne V]λλ3346,3426 emission lines in the Type 2 AGN is strong evidence for AGN activity.

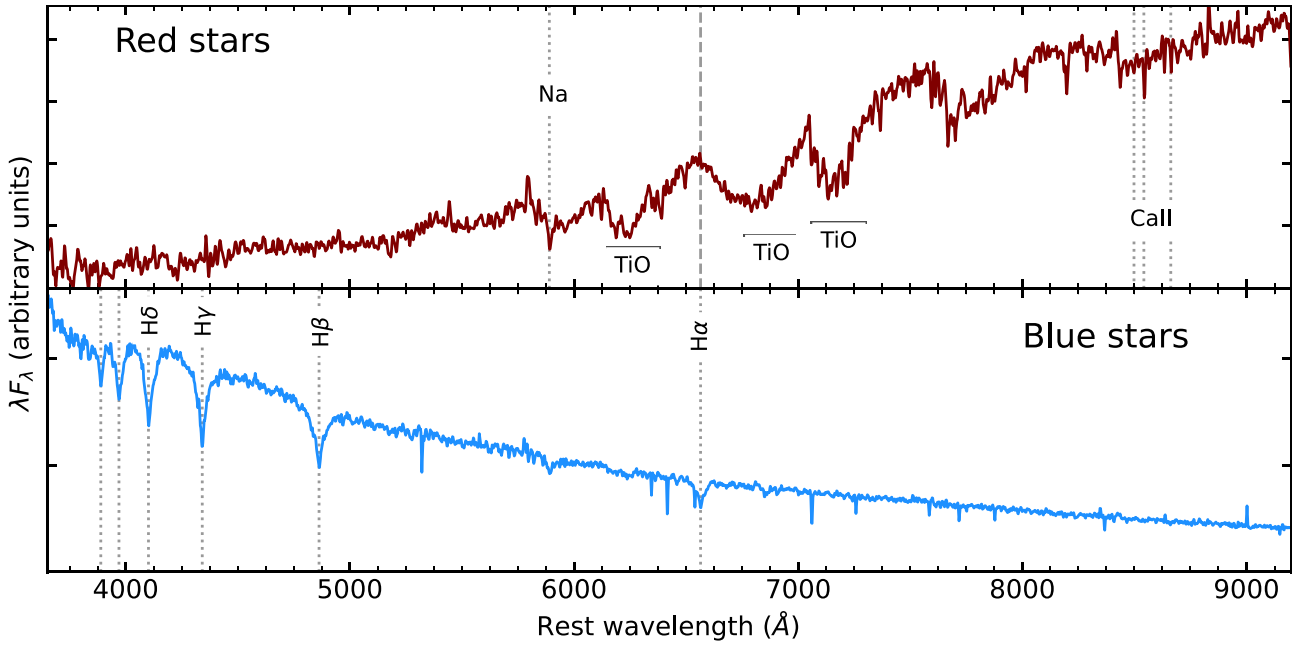

Figure B2. Composite of the 164 high-quality VI-confirmed stars in our DESI SP sample (see Section 2.1), split into red (top; $r - z > -0.4$, 142 stars) and blue (bottom; $r - z < -0.4$, 22 stars). The red stars show strong molecular features, indicative of red late-type stars (e.g. M-type), whereas the blue stars are mainly white dwarfs, as evidenced from the broad yet shallow Balmer absorption lines. The main emission and absorption features are indicated.

APPENDIX C: SDSS AND DESI COMPARISON

Matching our SP sample to the SDSS DR16 QSO catalogue (Lyke et al. 2020), we found 117 matches, of which 110 are considered high quality from the VI (107 are included in our SP QSO sample; see Section 2.1). For these 110 matches, we compared our VI redshifts and spectypes to that from the SDSS DR16 catalogue. Overall, seven sources have *significantly* different redshifts in SDSS to those obtained by the DESI VI ($\Delta z = |z_{\rm VI} - z_{\rm SDSS}|/(1 + z_{\rm VI}) \geq 0.05$; $\Delta v > 15\,000\,{\rm km\,s^{-1}}$), two sources were classified as Type 2 AGN in the VI and one additional source was classified as a galaxy in the VI, although all three had correct redshifts (see Table C1). For these ten sources, we performed additional VI to confirm the redshift and spectype; the seven sources with redshift disagreements had clearly incorrect SDSS redshifts (including one extreme high redshift BALQSO; see Table C1). The sources that were VI'd as a galaxy or Type 2 AGN have weak broad emission-line features.

Table C1. Table containing the SDSS ID, SDSS, and DESI VI redshift, and SDSS and DESI VI spectral type for the ten QSOs which either had a redshift or spectral type disagreement between the SDSS DR16 catalogue and that from the VI. †BALQSO.

	Redshift		Spectype	
SDSS ID	SDSS	DESI VI	SDSS	DESI VI
131 729.28 + 545 720.6	5.07	1.65	QSO	QSO
153 420.23 + 413 007.6	0.92	1.36	QSO	QSO
155 633.78 + 351 757.3†	1.49	3.24	QSO	QSO
155 921.70 + 435 700.6	0.66	1.36	QSO	QSO
160 113.56 + 422 637.7	0.15	1.72	QSO	QSO
163 148.98 + 495 933.4	4.53	1.45	QSO	QSO
170 016.63 + 350 353.5	4.50	1.39	QSO	QSO
142 843.33 + 120 913.3	1.19	1.19	QSO	GALAXY
143 827.41 + 370 737.3	1.01	1.01	QSO	QSO (Type 2)
130 100.88 + 320 727.4	0.51	0.51	QSO	QSO (Type 2)

APPENDIX D: TESTING THE RADIO DETECTION FRACTION PLOT

The key result of this paper is the striking positive correlation between the amount of line-of-sight dust extinction and the radio detection fraction (Fig. 10). To check the robustness of this result, we performed three tests (1) varying the MAD cut we imposed to define a 'good' spectral fit, (2) changing the redshift cut, and (3) exploring the 1.4 GHz FIRST and 3 GHz VLASS detection fractions (see Fig. D1).

For the first test, we applied three different MAD cuts: 4×10^{-5} (used for Fig. 10), 7×10^{-5}, and 20×10^{-5}, which were satisfied by ∼58 per cent (20 031/34 293), ∼ 85 per cent (29 001/34 293), and ∼ 99 per cent (33 913/34 293) of the combined QSOs, respectively. We find that relaxing the MAD cut slightly decreases the overall radio detection fraction, but does not change the shape of the trend; this demonstrates that the choice of MAD cut does not significantly affect our basic result. For the second test, we used a redshift cut of $0.5 < z < 2.0$ and $1.0 < z < 2.5$. The first range was chosen to exclude the highest redshift sources ($z > 2.0$) that may not have such reliable fits due to the limited rest-frame spectral coverage of our blue QSO composite used in the fitting and the second range excludes the lowest redshift sources ($z < 1.0$) that may still have contribution from the host galaxy (Section 3.3). We find that the overall trend is the same for both redshift ranges.

For the last test, we matched the combined QSO sample to the 1.4 GHz VLA FIRST and 3 GHz VLASS[23] surveys, adopting a 10 arcsec matching radius for both surveys which resulted in 5 per cent (1001/18 816; the sample was reduced to the FIRST survey area) and 2 per cent (631/34 293) matches, respectively. This is consistent with the sensitivity of FIRST (0.15 mJy) and VLASS (0.12 mJy); assuming a canonical spectral index of $\alpha = 0.7$, extrapolating the LDR2 flux values to 1.4 and 3 GHz, we expect 1079 and 882 QSOs to be detected in FIRST and VLASS, respectively. We find a positive trend in the FIRST radio detection fraction as a function of $E(B - V)$ out to $E(B - V) = 0.3$ mag, after which the source statistics are too limited to conclude anything meaningful (Fig. D1). This is despite FIRST being ∼9 times less sensitive than

[23]Note: for VLASS, we utilized the 'Host ID' table, which contains 700 212 sources that have relatively simple morphology for which a host has been identified using a maximum likelihood ratio. This has been found to be more reliable than the larger 'Component' table. The various tables can be found here: https://cirada.ca/vlasscatalogueql0

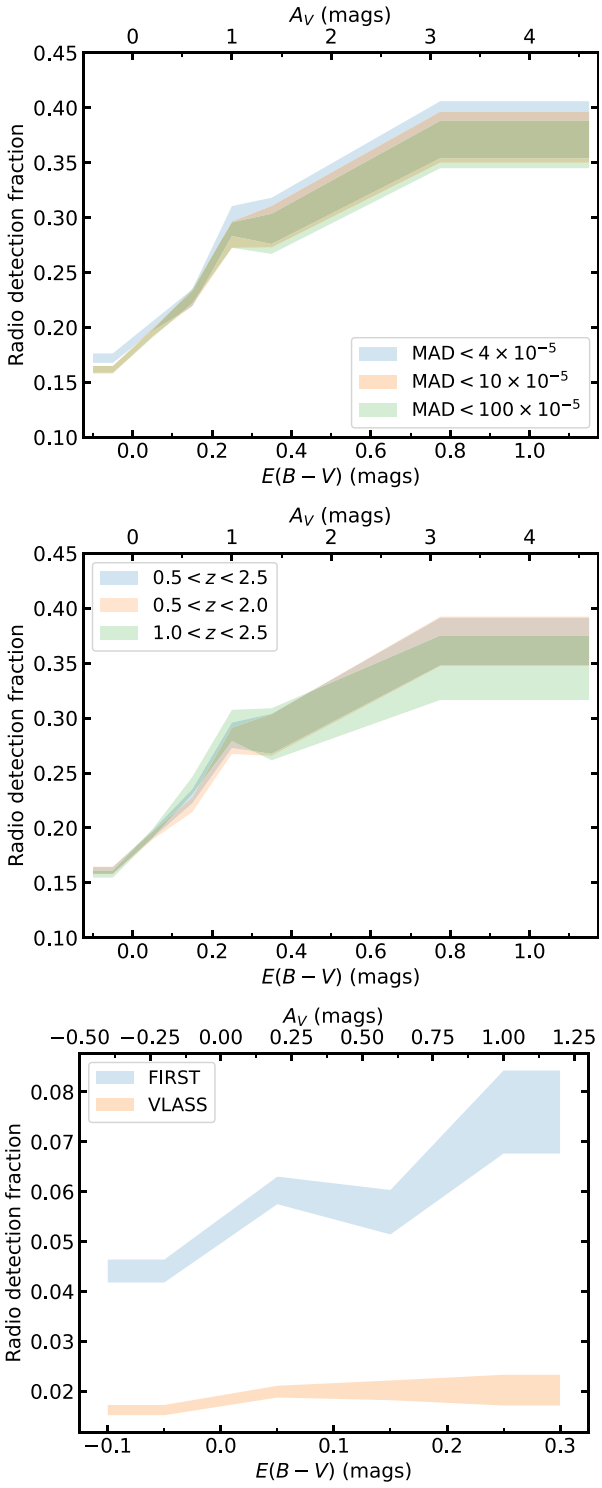

Figure D1. Similar to Fig. 10 with varying MAD cuts (top), varying redshift cuts (middle), and using both VLA FIRST and VLASS data (bottom). Overall, varying the MAD cut has little effect on the shape of the correlation. We find that applying a redshift cut of $0.5 < z < 2.0$ or $1.0 < z < 2.5$ does not affect the overall trend, although the source statistics are worse in the latter bin. Although limited by source statistics, the FIRST detection fraction also increases with increasing dust extinction [there are too few sources at $E(B - V) > 0.3$ mag to constrain the detection fraction]. The VLASS detection fraction shows a slight increase, but this is not significant due to the limited source statistics. Examples of dust extinction fits with a range of MAD values can be found in the online supplementary material.

Table D1. Radio detection fraction of the combined QSO table utilizing radio data from the LDR2, FIRST, and VLASS, adopting a matching radius of 5, 10, and 10 arcsec, respectively. To calculate the FIRST radio detection fraction the combined QSO sample was restricted to the FIRST survey region, reducing the sample to 18 816.

Radio survey	Radio detection fraction
LDR2	6549/34 293 (19 %)
FIRST	1001/18 816 (5 %)
VLASS	631/34 293 (2 %)

LoTSS, again adding to the robustness of our result. The VLASS radio detection fraction displays a subtle increase with $E(B-V)$, but unfortunately the source statistics are too low to robustly conclude anything. Table D1 displays the radio detection fractions of the combined QSO sample for LDR2, FIRST, and VLASS.

[1]*School of Mathematics, Statistics and Physics, Newcastle University, NE1 7RU, UK*
[2]*Centre for Extragalactic Astronomy, Department of Physics, Durham University, South Road, Durham, DH1 3LE, UK*
[3]*Department of Physics and Astronomy, The University of Utah, 115 South 1400 East, Salt Lake City, UT 84112, USA*
[4]*Department of Physics & Astronomy, University of Wyoming, 1000 E. University, Dept. 3905, Laramie, WY 82071, USA*
[5]*Lawrence Berkeley National Laboratory, 1 Cyclotron Road, Berkeley, CA 94720, USA*
[6]*Physics Dept., Boston University, 590 Commonwealth Avenue, Boston, MA 02215, USA*
[7]*Institute of Cosmology & Gravitation, University of Portsmouth, Dennis Sciama Building, Portsmouth, PO1 3FX, UK*
[8]*Department of Physics & Astronomy, University College London, Gower Street, London, WC1E 6BT, UK*
[9]*Instituto de Física, Universidad Nacional Autónoma de México, Cd. de México C.P. 04510, México*
[10]*The Ohio State University, Columbus, 43210 OH, USA*
[11]*Institut de Física d'Altes Energies (IFAE), The Barcelona Institute of Science and Technology, Campus UAB, 08193 Bellaterra Barcelona, Spain*
[12]*Departamento de Física, Universidad de los Andes, Cra. 1 No. 18A-10, Edificio Ip, CP 111711, Bogotá, Colombia*
[13]*Center for Cosmology and AstroParticle Physics, The Ohio State University, 191 West Woodruff Avenue, Columbus, OH 43210, USA*
[14]*Department of Physics, The Ohio State University, 191 West Woodruff Avenue, Columbus, OH 43210, USA*
[15]*NSF's NOIRLab, 950 N. Cherry Ave., Tucson, AZ 85719, USA*
[16]*Department of Physics, Southern Methodist University, 3215 Daniel Avenue, Dallas, TX 75275, USA*
[17]*Institució Catalana de Recerca i Estudis Avançats, Passeig de Lluís Companys, 23, 08010 Barcelona, Spain*
[18]*Department of Physics and Astronomy, Siena College, 515 Loudon Road, Loudonville, NY 12211, USA*
[19]*National Astronomical Observatories, Chinese Academy of Sciences, A20 Datun Rd., Chaoyang District, Beijing, 100012, P.R. China*
[20]*Department of Physics and Astronomy, University of Waterloo, 200 University Ave W, Waterloo, ON N2L 3G1, Canada*
[21]*Perimeter Institute for Theoretical Physics, 31 Caroline St. North, Waterloo ON N2L 2Y5, Canada*
[22]*Waterloo Centre for Astrophysics, University of Waterloo, 200 University Ave W, Waterloo ON N2L 3G1, Canada*
[23]*Space Sciences Laboratory, University of California, Berkeley, 7 Gauss Way, Berkeley, CA 94720, USA*
[24]*University of California, Berkeley, 110 Sproul Hall #5800 Berkeley, CA 94720, USA*
[25]*Steward Observatory, University of Arizona, 933 N, Cherry Ave, Tucson, AZ 85721, USA*
[26]*Department of Physics and Astronomy, Sejong University, Seoul, 143-747, Korea*
[27]*Institute of Space Sciences, ICE-CSIC, Campus UAB, Carrer de Can Magrans s/n, 08913 Bellaterra, Barcelona, Spain*
[28]*University of Michigan, Ann Arbor, MI 48109, USA*

This paper has been typeset from a TEX/LATEX file prepared by the author.